Durability of cracked SFRC exposed to wet-dry cycles of chlorides and carbon dioxide – multiscale deterioration phenomena

V. Marcos-Meson[1,2,3*], M. Geiker[4], G. Fischer[1], A. Solgaard[2], U.H. Jakobsen[5], T. Danner[6], C. Edvardsen[2], T.L. Skovhus[3] and A. Michel[1]

[1]Department of Civil Engineering, Technical University of Denmark, Kgs. Lyngby, Denmark

[2]COWI A/S, Kgs. Lyngby, Denmark

[3]VIA Building, Energy, Water & Climate, VIA University College, Horsens, Denmark

[4]Department of Structural Engineering, NTNU, Trondheim, Norway

[5]Danish Technological Institute, Taastrup, Denmark

[6]SINTEF, Trondheim, Norway

Abstract

This paper describes an experimental study that comprised the exposure of cracked SFRC members to wet-dry cycles involving chloride and carbon-dioxide for two years. Results indicate that corrosion of steel fibres occurs mainly at the outer regions of the crack for cracks smaller than 0.3 mm, where the pH inside the crack drops below values of nine. The presence of chloride affected mainly the extent of corrosion. The results indicate that corrosion damage of the steel fibres does not necessarily play a dominant role on the overall deterioration of the composite; since changes in the microstructure of the matrix surrounding the crack and the fibre-matrix interface due to leaching and autogenous healing, may have a substantial impact on the long-term behaviour of the cracked composite. A conceptual deterioration model was developed, describing the deterioration and recovery mechanisms that alter the long-term mechanical performance of the cracked composite under wetting-drying conditions.

Keywords

Steel Fibre Reinforced Concrete (SFRC), cracks, chlorides, carbonation, corrosion, petrography, healing

1. Introduction

Steel Fibre Reinforced Concrete (SFRC) is used in the construction of infrastructure exposed to aggressive environment that often involve exposure to chlorides and carbon dioxide. Previous studies generally agree regarding the good long-term performance of uncracked SFRC exposed to aggressive environments; but are inconsistent regarding the extent of fibre corrosion inside cracks and its impact on the tensile toughness of the cracked composite for cracks in the range of 0.1 – 0.3 mm [1].

To date, there is a limited understanding of the deterioration processes of cracked SFRC in aggressive media, such as saline or fresh water. Earlier research has in general based its conclusions on macroscopic observations relating the mechanical performance of the composite to the corrosion of the carbon-steel fibres [1]. It is not clear whether toughness variations reported after exposure are related solely to corrosion damage at the fibres or if additional changes in the fibre-matrix bond due to alteration of the concrete matrix during exposure also plays a role [2,3], as also discussed in [1,4]. Ongoing studies have shown that exposure of cracked SFRC to some corrosive

environments, e.g. wet-dry cycles of freshwater or saltwater, do not necessarily lead to a reduction of the mechanical performance of the cracked composite; and may even result on an increase of the mechanical performance over time [4]. Yet, those changes cannot be explained by a conventional deterioration model, which accounts mainly for the detrimental contribution of fibre corrosion [5,6]. Thus, more detailed deterioration models were proposed [1]; which, however, lack data to substantiate their hypotheses.

The deterioration process of the material reported in macroscopic observations of cracked SFRC is initially triggered by the transport of moisture and other chemical species (henceforth "species") inside the crack. However, transport of species in cementitious composites involves multiple concurring processes: diffusion and convective transport of moisture and species, dissolution of primary phases of the binder and precipitation of secondary phases in voids [7]. These processes are increasingly complex when cracking of the concrete matrix facilitates the transport through the main cracks [8–10] and into the damaged matrix adjacent to the crack [11,12]. Concurringly, the reactivity of the hardened cement matrix surrounding the crack alters substantially the structure and transport properties (e.g. ionic, moisture or gas) along the crack with time; due to, among others: leaching in the surrounding matrix [13], binding of species (e.g. Cl^-) [14,15], carbonation of the cement paste [16,17] and autogenous healing [18–20].

The transport and reaction processes previously described eventually yield conditions inside the crack (in terms of e.g. pH, RH, $[O_2]$, $[Cl^-]$) that shift the electrochemical potential of the exposed steel locally and may lead to corrosion of the steel fibres bridging the crack. Whereas, additional damage that propagates along the steel-matrix interface during pull-out [21–23] is expected to play a significant role on the corrosion of steel fibres in cracked concrete [1]. Yet, there is limited data to support a conclusive discussion and there is insight indicating that "self-healing" processes may restore part of this damage with time under certain exposures (e.g. wet-dry cycles); which would lead to a strength regain of the fibre-matrix bond over time [24,25].

The foregoing discussion reflects the overall complexity involved in the long-term performance of cracked SFRC subject to aggressive corrosive exposures. Potential deterioration to the properties of the cracked composite during exposure: e.g. structural and/or pervious; does not comprise a single developing process that can be predicted based on macroscopic observations. Instead, it requires a deeper understanding of several interconnected processes at various scales, which can lead in some cases to partial or total recovery of some of the properties of the bulk material.

2. Research significance and content

The aim of this study is to describe the main deterioration and recovery mechanisms observed in cracked SFRC subject to potential aggressive exposures and discuss its contribution to the long-term performance of the cracked composite. The paper presents the results of an experimental campaign investigating the durability of cracked SFRC exposed to wet-dry cycles of saltwater, freshwater and carbon dioxide for two years; and discusses the impact of these exposure conditions on the corrosion of the steel fibres bridging the cracks and the alteration of the matrix surrounding the crack.

The experimental results discussed in this investigation are presented in **Section 4** in the context of the main deterioration processes affecting the material, while the employed experimental methodology is discussed in detail in **Section 3.** The experimental results comprise data from five studies on analogous specimens, covering: i) the quantification of fibre corrosion at the composite scale by means of fibre counting; ii) ingress of chloride ions and decrease of pH inside the crack based on colorimetric profiles and water-soluble chloride measurements; iii) modification of the elemental composition of the matrix surrounding the crack after exposure based on X-ray fluorescence spectrometry mapping; and iv) investigation of changes in microstructure around the crack due to exposure based on a petrographic study. The processed experimental data is presented in **Appendix A**.

The discussion section (**Section 5**), describes the main processes taking place during the exposure of cracked SFRC to wet-dry cycles and how these processes are interconnected at various scales, based on the results presented in **Section 4** and results from similar studies. The main deterioration and recovery mechanisms are described indicatively in a conceptual deterioration model presented in **Section 5**, which reviews and updates the conceptual deterioration model proposed in [1] and discusses the engineering implications of the findings.

3. Methodology

The investigation comprised the preparation, exposure, mechanical testing and characterization of 220 SFRC specimens, cracked in three-point bending at 0.15 and 0.30 mm and exposed to wet-dry cycles for one and two years. The investigated exposures comprised chloride and carbon dioxide, inducing steel corrosion. The characterization of the extent of ingress of species and fibre corrosion comprised: descriptive statistics on the fibre distribution, visual inspection, chemical analyses and petrographic investigation. An overview of the samples, exposure and characterisation techniques is shown in **Table 1**.

For consistency, the results and discussion section will use the terminology described in [4]: The word "specimen" refers to a single sampling unit, the word "sample" refers to a group of specimens similarly exposed.

Table 1. Samples, exposure in wet-dry cycles and characterization techniques. Abbreviations given in brackets (x) is used for sample identification. After [4].

Sample id.	Crack width (w) [mm]	Wet cycle (s)	Dry cycle (c)	Age (A / B)	Characterization		
					Profiles	XRF	TS
w15 s0 c0 A	0.15 (w15)	Limewater (s0)	Air (c0)	1 year (A)	pH	-	-
w30 s0 c0 A	0.30 (w30)					-	-
w15 s0 c0 B	0.15 (w15)	Limewater (s0)	Air (c0)	2 years (B)	pH	-	-
w30 s0 c0 B	0.30 (w30)					-	X
w15 s3 c0 A	0.15 (w15)	3.5 wt.% NaCl (s3)	Air (c0)	1 year (A)	pH, $AgNO_3$, Cl^-_{ws}	-	-
w30 s3 c0 A	0.30 (w30)					-	-
w15 s3 c0 B	0.15 (w15)	3.5 wt.% NaCl (s3)	Air (c0)	2 years (B)	pH, $AgNO_3$, Cl^-_{ws}	X	-
w30 s3 c0 B	0.30 (w30)					-	-
w15 s7 c0 A	0.15 (w15)	7.0 wt.% NaCl (s7)	Air (c0)	1 year (A)	pH, $AgNO_3$, Cl^-_{ws}	-	-
w30 s7 c0 A	0.30 (w30)					-	-
w15 s7 c0 B	0.15 (w15)	7.0 wt.% NaCl (s7)	Air (c0)	2 years (B)	pH, $AgNO_3$, Cl^-_{ws}	-	-
w30 s7 c0 B	0.30 (w30)					X	X
w15 s0 c5 A	0.15 (w15)	Fresh water (s0)	0.5 vol.% CO_2 (c5)	1 year (A)	pH	-	-
w30 s0 c5 A	0.30 (w30)					X	X
w15 s0 c5 B	0.15 (w15)	Fresh water (s0)	0.5 vol.% CO_2 (c5)	2 years (B)	pH	-	-
w30 s0 c5 B	0.30 (w30)					X	X
w15 s3 c5 A	0.15 (w15)	3.5 wt.% NaCl (s3)	0.5 vol.% CO_2 (c5)	1 year (A)	pH, $AgNO_3$, Cl^-_{ws}	-	-
w30 s3 c5 A	0.30 (w30)					-	-
w15 s3 c5 B	0.15 (w15)	3.5 wt.% NaCl (s3)	0.5 vol.% CO_2 (c5)	2 years (B)	pH, $AgNO_3$, Cl^-_{ws}	-	-
w30 s3 c5 B	0.30 (w30)					-	-

Abbreviations: (Profiles) refers to the colorimetric profiles for Phenolphthalein and universal indicator "pH"; (XRF) refers to X-Ray Fluorescence mapping in polished specimens; and (TS) refers to polarized-light microscopy on polished Thin-Sections.

3.1 Preparation of specimens

The specimens were prepared with mixture proportions presented in **Table 2**. The total binder content was 426.3 kg/m^3, CEM-I was replaced by 31wt.% fly ash and the water-to-binder ratio (w/b) was 0.34,. The superplasticizer and air entrainer content were adjusted in the subsequent mixes to reach a slump of 100±20 mm and an entrained air content of 3.5±1.0 vol.% The steel fibre used was a cold-drawn hooked-ended fibre (type 1 according to EN 14889-1 [26]), made of cold-drawn high-carbon steel, with a length of 60 mm and a diameter of 0.75 mm.

The production of the specimens was done in a prefabrication plant, using an industrial mixing plant. The specimens were cast in three batches in consecutive days, demoulded after one day and sealed cured indoors, covered with plastic for 56 days at 20°C. Additional details of the production process are given in [27]. The final dimensions of the three-point bending beam specimens was 600 x 150 x150 mm, with a 25 mm notch cut at the centre, along the transversal direction, according to [28].

Table 2. Mix-design

Component	Quantity (kg/m^3)
Cement (CEM I 52.5N)	326.3
Fly Ash	100.0
Water	145.0
Sand 00/02	626.5
Sea gravel 04/08	175.1
Sea gravel 08/16	933.6
Steel fibres	40.0

3.2 Exposure setup

The exposure setup was built from ten plastic containers with a volume of 1 m^3, connected in pairs and alternating the wetting and drying cycle Specimens were exposed to wet-dry cycles of 2 + 2 days comprising different combinations of saturated limewater; sodium chloride solutions, (3.5 and 7.0 wt.% NaCl), and air with or without CO_2 (0.07 and 0.5 vol.% CO_2), named "air-exposure" and "carbonation exposure" respectively, as described in **Table 1** and [4].

The drying cycle for the air-exposed samples was run in the laboratory air with a forced ventilation system on each tank with a nominal flow of 93 m^3/h. The drying cycle of the carbonation exposure ran through a closed loop with nominal air flow of 93 m^3/h and utilized a cooler to extract moisture from the air flow before the inlet. The samples were placed vertically with the crack in horizontal position, leaving a minimum separation of 50 mm between samples to ensure air circulation inside the tank.

The water solution (hereafter "solution") was replaced every two weeks during the first three months of the exposure and then monthly until six months of exposure. After that, the solution was replaced every two months. The composition of the solution was checked through weekly measurements of Total Dissolved Solids (TDS) and pH. Additionally, the Cl^- concentration of the saltwater solutions was measured by spectrophotometry (Hach Lange DR3900 and reagent LCK311), before replacing the solution and was compared against the TDS values registered. The solution of the cracked references was not replaced, and a 20/80 mixture of saturated sodium and calcium hydroxide (pH = 13.5) was added weekly, keeping the pH value in the range of 10 – 13.5. The temperature and relative humidity inside the room were monitored, varying in the range 20±2 °C and 50±10 % respectively. The CO_2 concentration in the room and inside the carbonation loop were measured weekly and ranged approximately 0.07±0.01 % and 0.5±0.1% vol., respectively.

The specimens were cracked at 0.15 and 0.30 mm in 3-point bending before the exposure, measured at the crack mouth, following the procedure described in [4]. After one- and two-year exposure, the specimens were tested in 3-point bending. Further description of the mechanical-testing procedure and results can be found in [4].

3.3 Visual inspection, fibre counting and colorimetric profiles

After exposure and testing, the specimens were opened completely, and the fibres were counted and classified according to the degree of corrosion observed, see **Fig. 1**. The counting was made taking a digital image of the

surface of the sample, as shown in **Fig. 2b**. The fibres were marked using oil-based modelling clay with the following colour code:

- Level 1, no corrosion (green): the fibre does not present any signs of corrosion, there is no rust or corrosion pits observable at the surface at 2× magnification.
- Level 2, minor corrosion (yellow): the fibre presents rust spots at the surface with no visible loss of cross-section at 2× magnification.
- Level 3, moderate corrosion (orange): the fibre presents localized corrosion pits and moderate loss of cross-section, i.e. localized reduction of cross-section larger than approx. 20%. The fibre did not rupture during pull-out or rupture showed clear signs of load transfer, e.g. necking at rupture section.
- Level 4, severe corrosion (red): the fibre presents large pits and major or total loss of cross-section. The fibre does not present signs of transferring load during pull-out (i.e. necking at the steel cross-section is not observed).

Furthermore, colorimetric tests were done on the cracked surface to measure the penetration of free chlorides using $AgNO_3$ [29] and to estimate the carbonation depth and pH inside the crack using phenolphthalein and rainbow indicator [30], as shown in **Fig. 2c**.

The fibre count and calculation of ingress profiles was done on every replicate of each of the samples exposed. The data was combined and analysed in batches using an image analysis script [31], where fibres were counted combining colour segmentation on the image and posterior calculation of the centroids of each point in the mask, see **Fig. 2b**. Whereas the free chloride and pH profiles are presented discretized as a trapezoid containing the boundary of the colour indicator for each specimen, according to **Fig. 2c**.

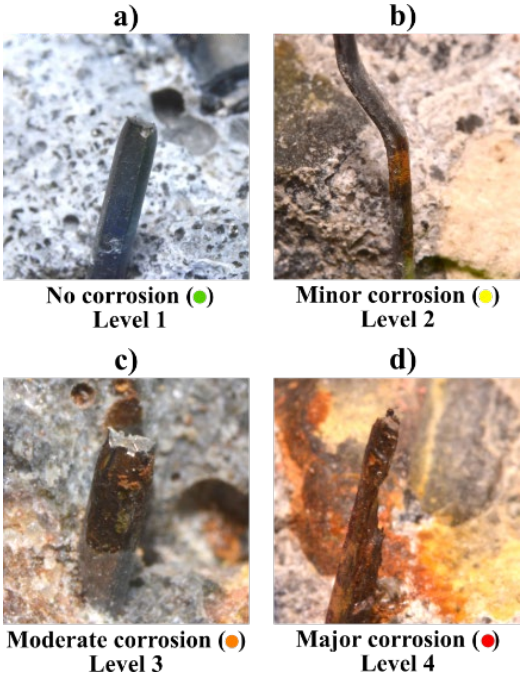

Fig. 1. Visual inspection, fibre classification: a) no corrosion (Level 1), b) minor corrosion (Level 2), c) moderate corrosion (Level 3), d) major corrosion (Level 4). After [4].

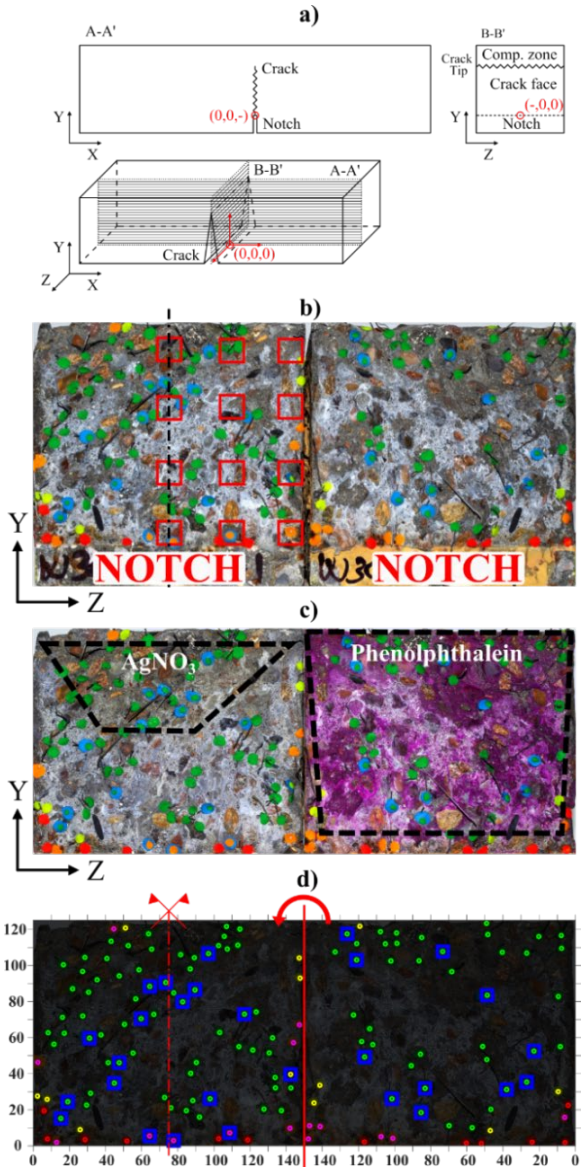

Fig. 2. Visual inspection and colorimetric analysis: a) specimen geometry and reference coordinates, b) crack surface and location of extraction points for grinding (red boxes); c) colorimetric indicators $AgNO_3$ for chloride detection (left) and e.g. the phenolphthalein for pH indication (right), and discrete profiles; and d) fibre counting and classification. After [4].

3.4 Water-soluble chloride profile inside the crack

The water-soluble chloride concentration inside the inner surface of the crack (hereafter "crack faces") was measured in one specimen of each sample, e.g. one of the split parts resulting from the complete opening of the test specimens of each sample.

The water-soluble chloride profiles were measured on dust samples, ground off from the surface of the crack, at the locations shown in **Fig. 2b**, on a 3x4 regular grid: at 0, 35, 70 mm from the centre of the crack in the x-axis and at 5, 35, 70 and 115 mm from the notch in the y-axis. Additionally, a sample was extracted at the surface of the specimen, at 0-1 mm depth.

The profile was grinded with a 5 mm spherical diamond drill bit, in an area of 10 x 10 mm area and to a depth of 0.2±0.1 mm, extracting a dust sample of 150±50 mg. The dust samples were leached in distilled water, by adapting the methods described in [32,33] as follows: i) approx. 100 mg was weighted to a 0.01 mg precision and 10 ml of

distilled water were added; ii) the suspension was stirred for 24 h at 20 °C; iii) the suspension was filtered and 0.5 ml of the filtrate were analysed by means of Ion Chromatography (Dionex Aquion from ThermoFisher Scientific). The chloride concentration was calculated to mg/g of dry material or wt.%

The water-soluble chloride profiles over the crack surface are calculated using 2-dimensional linear interpolation between the extraction points and were resampled to a 1 mm/pix resolution. Finally, the resulting profiles were smoothed using a 2-dimensional Gaussian convolution filter with $\sigma = 2$, see [34].

3.5 Elemental chlorine profile transversal to the crack

The elemental chlorine concentration in the cement paste was measured by means of micro X-ray fluorescence spectrometry mapping (μXRF), with the equipment and methods presented in [20] and data treatment following a similar methodology as [35]. Three specimens were analysed: the first specimen was used to investigate the ingress at two locations inside the crack, i.e. at the centre (coordinates x-y-0 mm in **Fig. 2a**) and at the edge (coordinates x-y-70 mm in **Fig. 2a**); the second and third specimens, were used to investigate the evolution of ingress at the centre of the crack (coordinates x-y-0 mm in **Fig. 2a**) with exposure time.

The first specimen was prepared after one-year exposure to wet-dry cycles with 3.5 wt.% NaCl solution. After the exposure, the specimen was dried in laboratory air for four weeks, and a 150 mm cube comprising the central section, i.e. at the location of the crack, was cut-off. Then, the crack was stabilized by vacuum epoxy-impregnation and was dry cut with a diamond saw, at two locations: at the centre of the crack and at 10 mm from the specimen face. The second and third specimen were prepared after one- and two-years of exposure to wet-dry cycles of 7.5 wt.% NaCl. The specimens were dried, cut and impregnated like the first one, but only at the centre of the crack.

The scanning was done on a Bruker® M4 Tornado, using a silver X-ray tube focused to a spot size of 25 μm and a silicon drift detector energy dispersive spectrometer (SDD-EDS). The elemental mapping was done at a current density of 600 μA and a voltage of 50 kV, with a chamber pressure of 20 mbar. The elemental mapping area was 120 x 120 mm. Mappings were taken with a speed of 1 ms/pixel for qualitative interpretation and 70 μm distance between each pixel. The resulting maps show percentage of the differential range measured, expressed as “counts”.

The calibration of the measured elemental composition was made by means of four specimens of cement paste (10mm diameter cylinders) prepared with the same cement used in the main experiments and a w/c = 0.35, cut and dry-polished to 5 mm diameter discs. The analysed specimens comprised: i) one specimen with no mixed-in NaCl, ii) three specimens with 1, 2.5 and 5 wt.% of mixed-in NaCl, diluted in the mixing water. The references were scanned together with the specimens using the μXRF technique previously described. The calibration was done by means of linear regression, assuming a linear calibration function with a zero constant; a coefficient of 0.0572 wt.%/count was calculated with an $R^2 = 0.99$. Finally, the elemental maps were post-processed to segment-out the regions covered by aggregates, steel fibres and epoxy resin (i.e. cracks, notch and voids), leaving the resulting matrix comprised of cement paste. Furthermore, it was found that the epoxy impregnation of the crack did not affect the segmented chlorine maps by scanning a cracked specimen exposed to freshwater.

3.6 Petrographic study

The preparation techniques used correspond to those described in [36,37]. The preparation process comprised the following: i) drying of beams under laboratory for 4 weeks, ii) cutting petrographic specimens from the central crack section (150 mm cube), iii) vacuum resin impregnation of the petrographic specimens to stabilize crack, iii) sawing of the petrographic specimen at the central section (i.e. 150 x 150 x 75 mm prism) and drying in oven at 35°C for approx. 10 hours, iv) vacuum resin impregnation of the sawed face and subsequent grinding, lapping and polishing to prepare polished-sections and thin-sections.

Optical polarizing microscopy was used to characterize the extent of leaching and carbonation inside the crack, quantify the changes in porosity, describe mechanical damage and characterize secondary phases formed in the crack. Thin-sections were analysed using a Leica DM2500P optical polarizing microscope equipped with a fluorescent facility. The fluorescent filter combination used was a BG12 excitation filter and a K530 yellow blocking filter, as previously utilized in [38].

An overview image of the thin-sections was scanned using an Epson V850pro flatbed film scanner at 2400 dpi and 24bit depth. Plane sections were photographed under UV light at 24.5 MP resolution using a 60mm f2.8D macro lens.

3.7 Statistical, numerical and image analyses

The results section includes two main types of statistical analyses: comparison of samples based on the Student's t-test, used in Sections 4.1, 4.2 and 4.4, and a regression model used in Section 4.5.

The analysis of fibre corrosion and threshold values (**Section 4.1.3**) is based on the numerical interpolation to calculate the pH and Cl^- profiles for each specimen. The pH and water-soluble Cl^- concentration inside the cracks were calculated for every specimen using the pH profiles and water-soluble Cl^- data presented in **Appendix A**. First, the values of water-soluble Cl^- extracted from dust samples were recalculated to concentrations in the solution inside the crack, assuming a 1-1 ratio between the dry binder and surrounding solution inside the crack, based on the discussion presented in [32]. Whereas, pH values were assumed from the colorimetric profiles. Second, the pH and Cl^- profiles discussed in **Section 4.1.3** were correlated to the abovementioned results to reconstruct the $[OH^-]$ and $[Cl^-]$ profiles inside the crack of each specimen, using numerical correlation and interpolation based on digital-inpainting with the algorithm developed in [39].

The porosity change due to secondary reactions in the cement paste is discussed in **Section 4.1**. The analysis is based on the comparison of the relative luminance histograms of UV fluorescence images, calculated from the RGB space, see e.g. [37]. The subsequent discussion is based on descriptive statistics of the data, compared to a reference cement paste from an uncracked specimen.

4. Results

The results of the investigations presented in this paper are discussed in the context of a conceptual deterioration model, derived from the discussion in [1], and presented indicatively on a time-scale in **Fig. 3**. The overall damage at the composite is described as the "global deterioration", being a combination of various deterioration and recovery processes that take place simultaneously at the composite. The concept of global deterioration may correspond to, for example variations on the mechanical performance of the cracked composite or on its permeability to fluids.

The deterioration processes affecting the performance of the cracked composite comprise: i) Transport of species, involving: external aggressive agents into the crack and adjacent matrix (e.g. Cl^- or CO_2) and transport of ions from the pore solution to the exterior (e.g. OH^- and Ca^{++}); ii) Alteration of the cement paste matrix due to non-equilibrium between solids and pore solution; and iii) Corrosion of the steel fibres bridging the crack.

The recovery processes comprise: i) The transport of species transverse to the crack faces towards the unaltered cement paste, which smears the bulk ionic concentration of those species over a larger volume; and ii) The dissolution of primary cement phases, which maintains equilibrium conditions inside the crack releasing (e.g. OH and Ca^{++}), the binding of aggressive species by the surrounding cement paste (e.g. chloride binding or neutralization of carbonic acid), and the precipitation of secondary phases inside cracks and voids

Following this conceptual model, individual processes (i.e. represented as linear trends in **Fig. 3**) which are described based on specific experiments, would result in a highly non-linear global deterioration process, which may not be realistically understood and predicted based on macroscopic observations; such as mechanical experiments of exposed specimens, as discussed in [1]. Furthermore, even if most of the deterioration processes described are irreversible, the combination of those with recovery processes may lead to the effective partial- or full-recovery of some properties of the cracked composite, such as its mechanical performance or its perviousness.

The results section herein focuses on describing these processes, based on selected results from the experimental data presented in **Appendix A**. The results are presented in two sections, covering deterioration and recovery processes respectively.

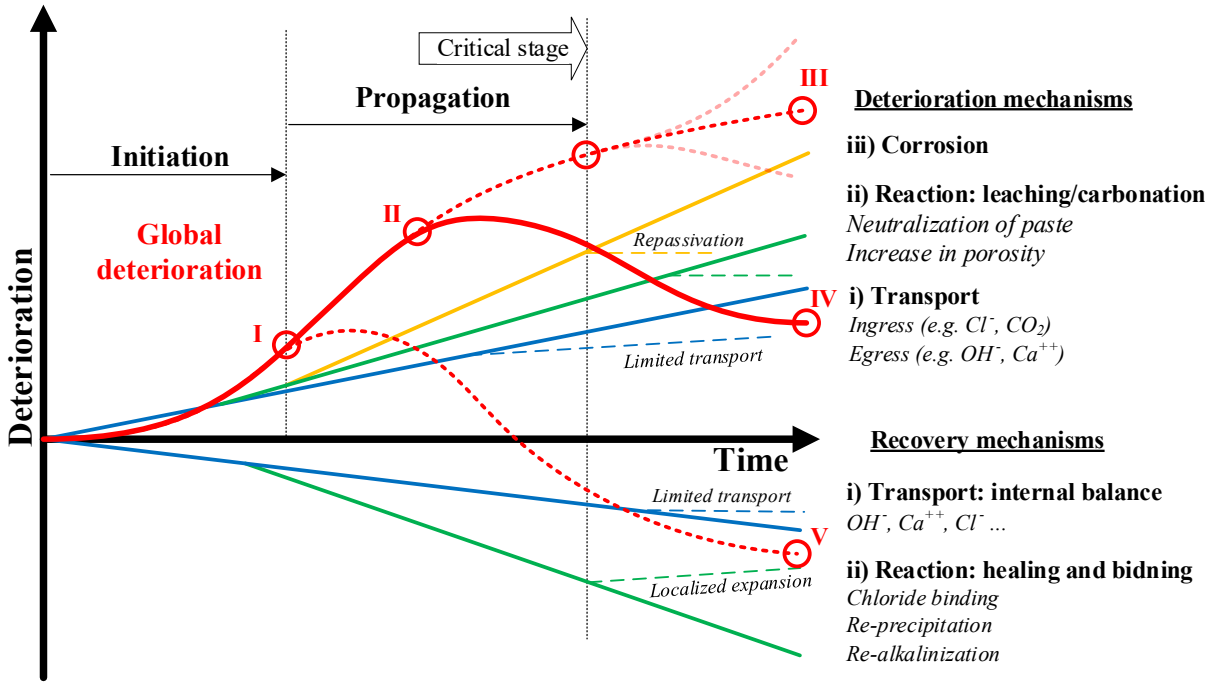

Fig. 3. Conceptual deterioration model. Individual mechanisms are separated into deterioration and recovery processes and are depicted as linear processes, while the global damage process is presented as a non-linear process. Distances and trends presented in the graphic are indicative. Roman numbers indicate relevant points of the global deterioration process in time, "stages", discussed in detail in **Fig. 12**.

4.1 Deterioration processes

The processes described in this section comprise alteration of the matrix surrounding the steel fibres, which are affected by: i) the transport of species through the crack, both ingress of extrinsic into the adjacent cement matrix and egress of intrinsic ions from the pore solution of the adjacent cement matrix; ii) the alteration of the microstructure and composition of the cement solid matrix, and iii) corrosion of the steel fibres.

4.1.1 Transport of species through the crack

Transport of species in uncracked concrete is typically obstructed by the complex and tortuous pore structure of cement paste. Whereas, cracks represent a preferential path for transport of moisture and species from and into the bulk concrete matrix. The results presented in this study cover the exposure to wet-dry cycles, leading to a complex transport scenario, which involves both diffusive and advective transport of dissolved species.

As a result, concentration of extrinsic species localizes at the outer regions of the crack. For example, the Cl^- and total Cl profiles show a tendency for large Cl contents at the outer 20 mm of the crack, i.e. approximate values of $[Cl^-]_{ws} \approx 0.6$ wt.%-cem and total Cl ≈ 2 wt.%-cem; which fall progressively at deeper zones of the crack (experimental data may be found in **Fig. 14** and **Fig. 15** in **Appendix A**). Additionally, the precipitation of carbonates inside the crack was only observed at the outer 20 – 40 mm, suggesting that transport of gaseous species may be limited along the depth of the crack (e.g. see description of petrographic data in **Fig. 16** in **Appendix A**).

Egress of intrinsic species (e.g. Ca and OH^-) was well observed in the thin-sections as leaching of the cement paste surrounding the crack, mainly at the outermost 20 – 40 mm of the crack, this phenomena is discussed further in **Section 4.1.2**.

The resulting decrease of several orders of magnitude in the $[OH^-]$ at the outer 20 – 30 mm inside the crack (i.e. from pH 14 to pH 9) was well observed in the pH profiles, e.g. that can be observed in data from **Fig. 13** in **Appendix A.** However, elemental maps for the main elements composing cement (e.g. Ca, Al, Fe, K and S) investigated by XRF (not presented in this publication) did not show such a large drop of these elements along the crack.

The main implications of these processes to the overall performance of the cracked composite are related to: i) changes in the concentrations of $[OH^-]$ and/or $[Cl^-]$ in the solution inside the crack, leading to corrosion of the steel fibres; and ii) alteration of the microstructure of the matrix adjacent to the crack, which leads to changes in the transport properties of the matrix and alterations of the fibre-matrix bond, e.g. as discussed in [4] for corresponding specimens to the ones described in this study.

4.1.2 Alteration of cement paste microstructure

Macroscopic observations of cracked specimens revealed a white precipitate covering the entire crack face, fading at the compression zone, see **Fig. 4**. The appearance and coloration of the precipitate changes at the outer 10 – 30 mm of the crack, at the boundary where the pH drops below pH 9, i.e. the Phenolphthalein threshold, see **Fig. 4b**. This region also comprises the area where fibre corrosion is typically observed. The area increases with longer exposure time and for larger crack widths.

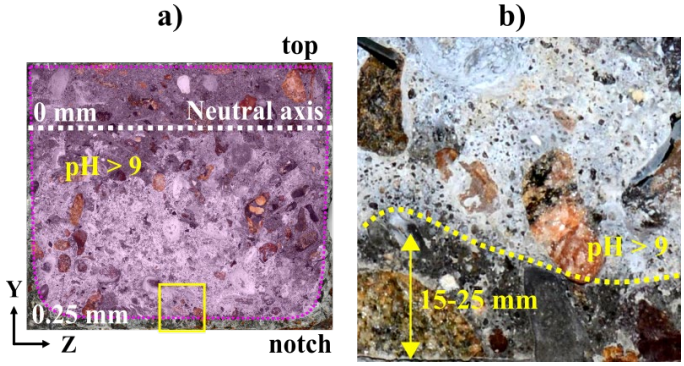

Fig. 4. Precipitate inside crack (on the crack faces), detail of coloration at outer edge. a) schematic view, b) image for 0.3 mm crack exposed to freshwater cycles for two years (w30s0c5).

In addition to changes in pH and chloride content, the extent and nature of the transformation of the matrix adjacent to the crack has been characterized by means of a petrographic study on thin-sections, (an overview is shown in **Appendix A**, **Fig. 16**), comparing the average luminance values at selected areas ($\bar{L}_i$) to the average luminance values on a reference specimen ($\bar{L}_{ref}$), i.e. a thin-section of an uncracked specimen exposed to limewater cycles for two years (s0c0B). Luminance values are presented in subsequent figures as the ratio ($\Delta_L = \bar{L}_i / \bar{L}_{ref}$), where values higher than 100% represent an increase in voids (i.e. porosity or damage) and smaller values represent a decrease.

The results presented in **Fig. 5** show the deterioration of the cement paste of the specimen exposed to 7 wt.% NaCl for one year, s7c0A. Results are presented at three locations inside the crack: i) at the crack mouth in **Fig. 5a**, ii) at 10 mm inside the crack in **Fig. 5b**, and iii) at 30 mm inside the crack in **Fig. 5c**.

The results show that there is substantial leaching and carbonation of the cement paste near the crack mouth, entailing an increase of the porosity at the region, see coloration in cross-polarized image and UV luminance in **Fig. 5a**. The thickness of the area around the crack that presents leaching and carbonation of the cement paste decreases gradually inside the crack, i.e. up to approx. 200 µm around the crack at 10 mm depth, see **Fig. 5b**. Whereas, at approx. 30 mm depth inside the crack, the cement paste surrounding the crack does not show significant deterioration due to leaching (see **Fig. 5c**).

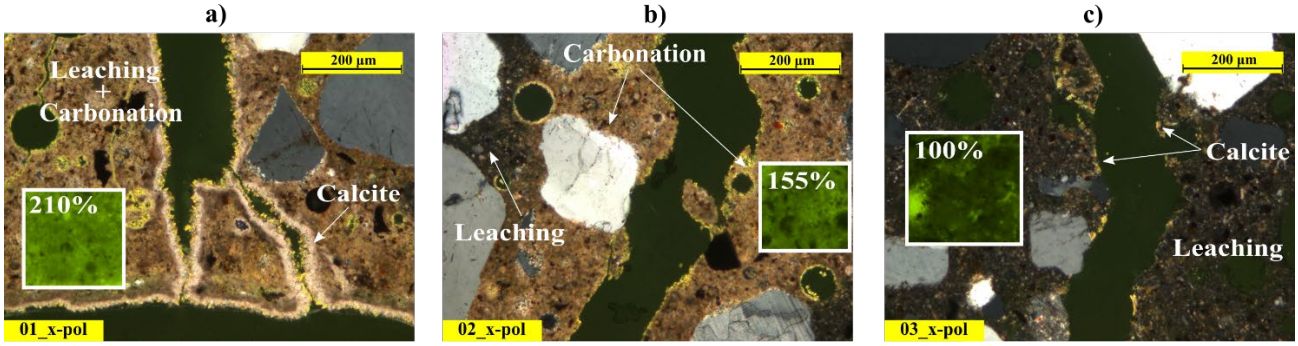

Fig. 5. Leaching and carbonation of cracked specimen exposed to 7% NaCl, w30s7c0A, inspection images at: a) crack mouth under cross-polarized light and UV fluorescent light; b) 10 mm inside crack under cross-polarized light and UV fluorescent light; c) 30 mm inside crack under cross-polarized light and UV fluorescent light. Mean luminance variation values under fluorescent light ($\Delta\bar{L}$) for selected areas shown as numbers in brackets.

The deterioration observed at the fibre-matrix interface and areas surrounding steel fibres are presented in **Fig. 6**. The figure shows the embedded region of two fibres that cross the crack: i) a fibre located at 15 mm inside the crack, at approx. 5 mm from the crack face **Fig. 6a**, and ii) at 40 mm inside the crack, at approx. 5 mm from the crack face **Fig. 6b-c**. Exact locations for these micrographs are given in **Appendix A** (**Fig. 16**).

As the main crack is generated in the matrix, the fibres bridging the crack are partially pulled-out from the matrix, which transfer the strain through as micro-cracking and crushing at the interface, see **Fig. 6a,b**; in particular at the hooked-ends of the fibre, see **Fig. 6b**. Such damage is expected to increase significantly the connectivity of the matrix surrounding the fibre through the micro-cracks (i.e. approx. 1 – 5 µm) to the main crack, as shown in the local changes of luminance following the fibre path in **Fig. 6b**. The aspect of the cracks presented in this paper corresponds well to observations on single-fibres reported in [21–23,40,41].

Observations for fibres located at the outer 10 – 40 mm of the crack after one- and two-years of exposure did not show a substantial impact of leaching and ingress on the microstructure of the matrix around the fibre. Yet, there were some local areas around cracks and pores where there was a significant increase in porosity, see UV luminance values in **Fig. 6a**. Localized damage at the fibre-matrix interface did not seem to induce a substantial transformation of the bulk cement paste adjacent to the fibre (see **Fig. 6b**). Despite that there was a narrow zone directly in contact to the steel surface, i.e. approx. 1 – 5 µm, rich in portlandite that showed in some cases a higher porosity compared to the bulk paste, see UV luminance values in **Fig. 6c**.

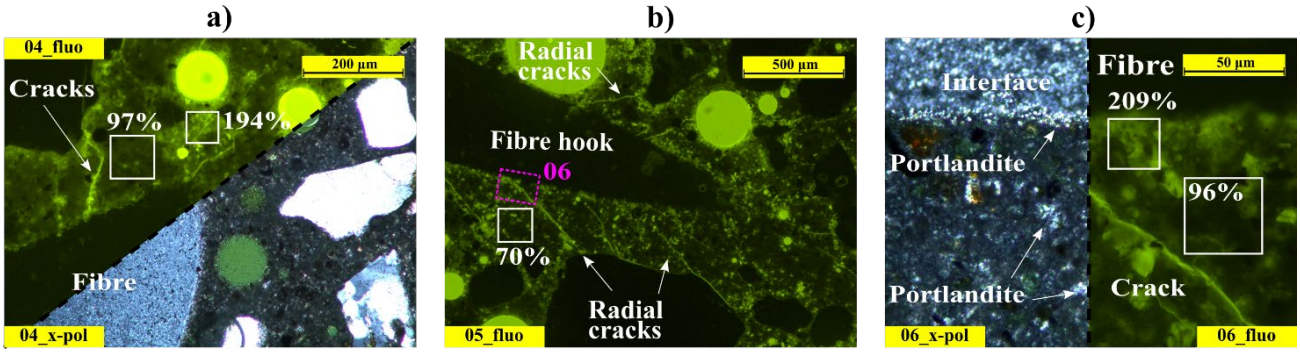

Fig. 6. Damage and leaching at fibre-matrix interface for: a) steel fibre bridging crack of specimen w30s7c0B, under cross-polarized and UV fluorescent light; b) steel fibre bridging crack of specimen w30s0c5B, under UV-fluorescent light; and c) detail of lower part of corresponding fibre presented in "b" under cross-polarized light and UV-fluorescent light. Mean luminance variation values under fluorescent light (ΔL) for selected areas shown as numbers in brackets.

4.1.3 Fibre corrosion inside the crack

The conditions inside the crack leading to fibre corrosion have been plotted in **Fig. 7** as the pH (x-axis) and water-soluble chloride concentration $[Cl^-]_{ws}$ expressed in mmol/l (y-axis), at the location of each fibre, based on the experimental data presented in **Appendix A** (see **Fig. 13** and **Fig. 14**). The fibres are plotted as dots, categorized in colours by the level of corrosion, as described in **Fig. 1**. Additionally, the results are compared to threshold values for initiation of corrosion in fibres exposed to chlorides proposed in former studies for embedded fibres [42] and fibres tested in artificial pore solution [5], which have been plotted as dotted and dashed lines. Fibres not exposed to chlorides were included in the plot, assuming a $[Cl^-]_{ws}$ = 2.5 mmol/l at the surface, equal to the values measured in the freshwater solution used.

The results presented in **Fig. 7** show that there is a correlation between the pH and $[Cl^-]_{ws}$ values measured in specimens exposed to chlorides, i.e. note the shape of the distribution of points, which mostly cover the upper-right diagonal of the plot. Such correlation is expected since the ingress of Cl^- and egress of OH^- are complementary transport processes that lead to higher $[Cl^-]_{ws}$ and lower pH values at the outermost regions of the crack, which decrease and increase correspondingly deeper into the crack. A similar discussion was presented in [5] for fibres embedded in concrete exposed to chlorides, which observed fibre corrosion at the outer 10 mm of the crack, and did not consider the $[Cl^-]_{ws}$ as the main factor contributing to corrosion.

Corrosion of steel fibres exposed to chlorides occurred primarily at pH values below pH 10 – 11, corresponding to $[Cl^-]_{ws}$ values of 80 – 100 mmol/l. Those results correspond reasonably well to threshold values for fibres embedded in concrete presented in [42], i.e. $[Cl^-]/[OH^-] \approx 320$. However, these are significantly higher than the threshold values for depassivation of steel fibres in pore solution presented in [5], which correspond to $[Cl^-]/[OH^-] \approx 2.5 – 50$ for pH values in the range 10 – 13.

Furthermore, the comparison of the abovementioned results to those for fibres not exposed to chlorides shows that overall the pH at the location of the fibre might be the dominant factor among the two, see values at $[Cl^-]_{ws} \approx 2.5$ mmol/l in **Fig. 7**. Noting that the presence of chloride leads to more severe corrosion damage at the exposed fibres and a larger number of fibres corroding compared to fibres not exposed to chlorides.

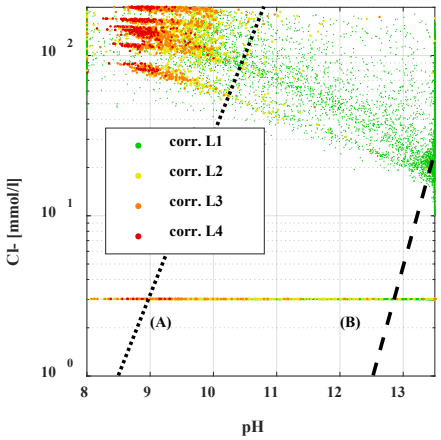

Fig. 7. Fibre corrosion (corrosion level L1 to L4) vs pH vs $[Cl^-]_{ws}$ for specimens exposed to chlorides and fresh water. Measured values are compared with threshold values proposed for: (A) fibres embedded in concrete [42] and (B) fibres tested in pore solution [5]. The specimens not exposed to chlorides included in the plot are plotted for a $[Cl^-]_{ws}$ = 2.5 mmol/l, plotted horizontally in the lower edge of the plot.

Petrographic observations of steel fibres embedded in uncracked concrete have shown that chloride-induced corrosion of fibres primarily appears at voids or defects at the steel-matrix interface, provided that the fibre is close to the surface, see **Fig. 8a**. No signs of spalling or substantial cross-sectional reduction were identified for fibres embedded in uncracked concrete in this study. These observations in thin-sections are in agreement with macroscopic observations and results reported in [43,44].

There was no consistent observation of localized corrosion at the deformed regions of the fibres (i.e. at the hook), which was only visible in a few fibres; which contradicts the observations form previous studies in uncracked [45] and cracked SFRC [46]. Whereas, the deterioration phenomena reported in this paper still agrees with the corrosion initiation and propagation mechanisms described at smaller scales in [5].

Corrosion of fibres in contact with the external environment (i.e. fibres at the surface or crossing cracks) occurred mainly at the exposed steel surfaces regardless of the presence of chlorides (**Fig. 8b)**. Corrosion did not extend deep inside the composite and did not cause any further damage to the matrix, i.e. cracking or spalling, similarly to what was observed in [43]. Corrosion of fibres crossing the cracks was localized at the intersection with the crack, and the adjacent 1 – 2 mm embedded in the matrix, as shown in the examples presented in **Fig. 1**. Petrographic observations presented in **Fig. 10** show that corrosion spots form at surfaces exposed to the crack, but carbonate precipitation and corrosion products tend to block those paths when exposed to wet-dry cycles.

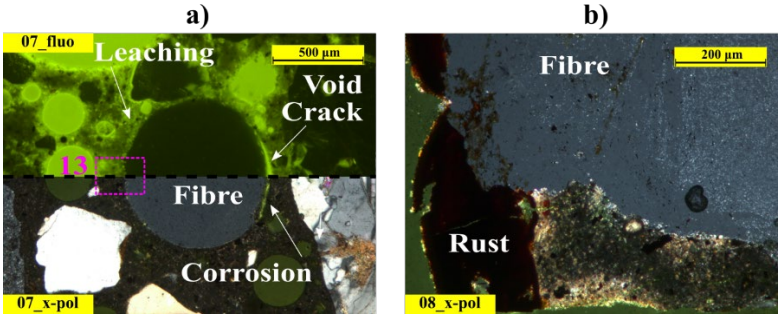

Fig. 8. Corrosion of steel fibres on: a) fibre embedded in the matrix at approx. 10 mm from the surface and exposed to chlorides, in specimens w30s7c0B, under cross-polarized light and UV-fluorescent light; and b) fibre directly exposed at limewater solution, in specimen w30s0c0A, under cross-polarized light.

4.2 Recovery processes

Based on the conceptual deterioration model proposed in **Fig. 3**, there are recovery processes opposing the deterioration processes, which prevent and reduce the extent of damage of the cement matrix and are expected to have a positive effect on the resistance to transport and/or mechanical performance of the cracked SFRC.

The processes described in this section comprise structural changes at the bulk matrix and at the matrix surrounding the steel fibres and are affected by three mechanisms:

i) Transport of species inside the bulk matrix which both reduce the concentration of aggressive species in the solution at the crack, and maintain a high pH in the pore solution at the crack
ii) Binding of aggressive ions at the cement matrix around the crack, that reduce the bulk concentration at the solution in the crack, and release of hydroxyl ions from cement phases that maintain high alkalinity
iii) Precipitation of secondary phases in pores and cracks that reduce moisture and ionic transport in the micro-cracked matrix

4.2.1 Transport of species within the matrix

The main crack serves as a preferential path for transport of species into the matrix adjacent to the crack. These processes, discussed in **section 4.2.1**, comprise a complex combination of diffusion of dissolved and gaseous species, advection of dissolved species and transport of moisture. Yet, the transport of species does not only take place inside the main crack, the matrix surrounding the crack is expected to play an important role for the overall concentration of dissolved species inside the crack.

As extrinsic ions are transported inside the crack, e.g. Cl^-, a concentration gradient relative to the adjacent matrix will promote the diffusion of those ions deeper into the matrix. Thus, lowering the bulk concentration of these inside the crack and distributing these species over a larger paste volume. This effect was well observed on the elemental Cl maps obtained from the XRF investigations (e.g. refer to XRF data presented in **Appendix A, Fig. 15**), where the elemental Cl content inside the crack decreases progressively both along and transversal to the crack, i.e. approx. 10 – 15 mm into the matrix surrounding the crack.

The aforementioned transport processes are generally competing with the bulk transport processes inside the crack, described in **Section 4.1.1**. However, the matrix adjacent to the crack comprises a large volume of pores that act as a "buffer" to the transport inside the crack, which generally slows the bulk ingress of aggressive species (e.g. Cl^-) and maintains stable concentrations of intrinsic species (e.g. OH^-).

4.2.2 Reactivity of the matrix: binding of Cl^- and release of OH^-

The cement matrix surrounding the crack reacts with the solution inside the crack, maintaining chemical equilibrium. Therefore, acting as a chemical buffer of dissolved species, that maintains stable concentrations of extrinsic ions (e.g. Cl^-) by means of binding processes, and intrinsic ions (OH^-) through dissolution processes.

First, the transport of Cl^- trough the crack and subsequent transport and binding into the matrix is well observed in the experimental data presented in **Appendix A** (e.g. **Fig. 14** and **Fig. 15**). Water-soluble chloride values measured at the faces of the crack reached values up to approx. 0.5 – 0.6 wt.%-cem at the outermost locations, decreasing up to values close to 0.01 – 0.05 wt.%-cem deeper inside the crack. Corresponding values for total Cl reached values in the range 1.5 – 2.5 wt.%-cem, reaching still moderate Cl content in the cement paste adjacent to the crack at deeper regions after two-years exposure (i.e. Cl ≈ 0.1 – 0.2 wt.%-cem).

Comparison of the total vs free chloride data shows that the total chlorine-to-water soluble chloride ratio ($[Cl]/[Cl^-]$) reaches values in the range $[Cl]/[Cl^-] \approx 2 - 4$ at the outermost 10 mm of the concrete, whereas these values

decrease down to $[Cl]/[Cl^-] \approx 1 – 1.5$ deeper inside the crack. There is therefore still substantial capacity for binding of Cl^- in the cement paste surrounding the crack, which may delay chloride-induced corrosion initiation of the steel fibres. Yet, this discussion does not aim at describing these processes in detail, being the reader aware of the large complexity of the binding and transport mechanisms involved in Cl^- ingress in concrete [7].

Secondly, alteration of equilibrium conditions in the pore solution at the matrix adjacent to the crack lead to the dissolution of primary phases (e.g. portlandite or sulfoaluminates), as described in **Section 4.1.2**; which result in the release of intrinsic ions (e.g. OH^- and Ca^{2+}) that enforce equilibrium conditions inside the matrix and at the crack. There is insight of this behaviour in the data presented in **Fig. 5**, which shows leaching of portlandite in the matrix adjacent to the crack, particularly at the outer 10 – 20 mm of the crack.

These recovery mechanisms generally contribute to stabilize the bulk ionic concentration of ionic species of the pore solution, and counteract the bulk transport processes (i.e. ingress and leaching) inside the crack, described in **Section 4.1.1**. Ultimately, these contribute to prevent corrosion of the steel fibres inside the crack.

4.2.3 Precipitation of secondary phases

The ingress of extrinsic species (e.g. Cl^- or CO_2) and dissolution of primary phases lead, under some conditions to the precipitation of secondary phases, typically inside moist voids and cracks. Macroscopic observations presented in **Fig. 4** show a precipitate covering the entire section of the crack for all the exposed specimens, regardless of the exposure type. The composition of this precipitate varies from a primarily carbonate phase at the outermost regions of the crack, to mostly ettringite and some ASR gel (i.e. from mechanically-fractured aggregates) deeper inside the crack.

The structure of the precipitate did not close entirely the crack throughout the whole section under any of the investigated exposures. Further investigation inside the crack, showed that initially fibre reinforcement may have reduced the average crack width substantially due to branching and splitting of the main crack into smaller ones, see **Fig. 9a**; as well as due to blocking of the crack locally with debris from the cracking process, see **Fig. 9b**. During exposure, both narrow cracks and debris tend to be preferential locations for precipitation of calcite and ettringite, as shown in **Fig. 9a**; which reduce the connectivity inside the crack and therefore hinder ionic and moisture transport. Precipitation of calcite occurred preferentially at the outer region of the main crack under salt-water (see **Fig. 5c**) and fresh-water exposure (see **Fig. 9c**), and blocked almost completely the access of moisture and ions to the crack; but it was minimum for specimens exposed to limewater.

Deeper inside the crack mostly ettringite formed (see **Fig. 9a)**, which did not seem to impede transport of moisture and ions but served as a preferential location for the precipitation of portlandite and calcite, likely limiting transport inside the crack. At these regions, there was also a thin layer of ASR gel lining parts of the crack, typically near the surface of some reactive aggregate that was mechanically fractured or exposed to the crack before the exposure, see **Fig. 9b**. Yet, this was not expected to have any significant impact on the transport through the crack or in the overall integrity of the cracked composite.

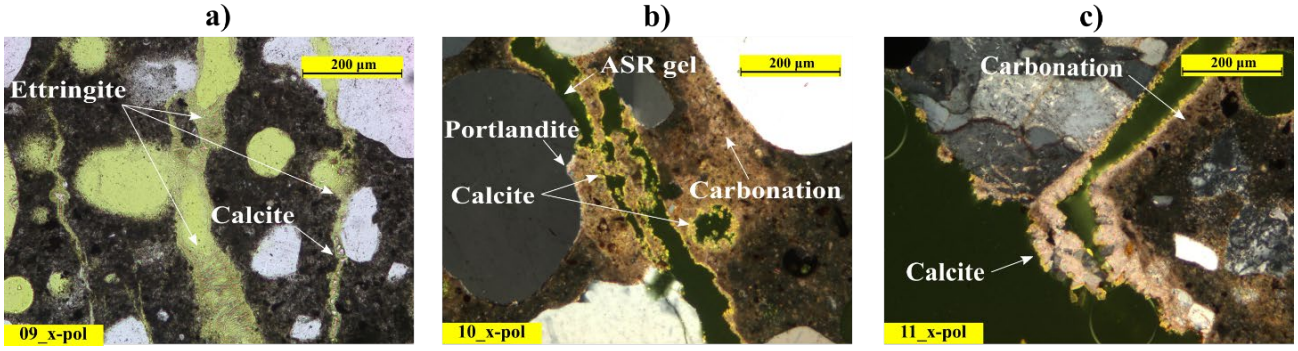

Fig. 9. Recovery phenomena inside cracks, showing precipitation of secondary phases at selected locations: a) calcite precipitation and carbonation at debris blocking partially the crack at 7mm depth observed under cross-polarized light, for specimen w30s0c0A; b) formation of ettringite needles at 28 mm inside the crack observed under polarized light, for specimen w30s7c0B; c) precipitation of calcite at crack mouth under cross-polarized light, for specimen w30s0c5B.

Precipitation of secondary phases also occurred around fibres crossing the crack, shown in **Fig. 10**, which covered partially the exposed surface of the fibre, but did not fully isolate the steel surface from the solution inside the crack.

Leaching from the adjacent matrix is expected to provide sufficient Ca^{2+} to facilitate the precipitation of calcite observed, as noted by the lower quantity of CH in the non-carbonated paste around fibre and lower density of paste under fluorescent light in **Fig. 10a**. Furthermore, precipitation of calcite sealed with time the main crack at discrete locations around the fibre, as observed in **Fig. 10c**, therefore reducing substantially the transport around the steel surface.

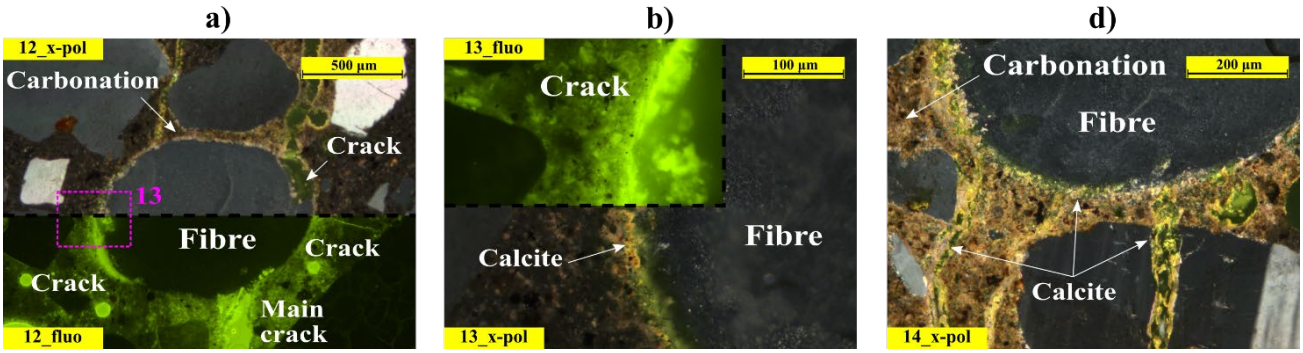

Fig. 10. Recovery phenomena at fibres crossing the crack, showing precipitation of secondary phases at selected locations: a) fibre crossing crack at 15 mm depth for specimen w30s0c5B, under cross-polarized light and UV-fluorescent light; b) detail of left part of corresponding fibre presented in "a" under cross-polarized light and UV fluorescent light; c) fibre crossing crack at 20 mm depth, for specimen exposed to limewater, w30s0c0A, under cross-polarized light.

The results reported in this study give insight on the formation of secondary phases at the fractured fibre-matrix interface of fibres crossing the crack near the crack region, yet the composition and formation mechanisms are not clear, see **Fig. 11**.

Initially, the interface of a fibre not crossing the crack showed a similar structure compared to the bulk matrix, except for a slightly larger concentration of portlandite at the adjacent 20 – 50 µm, as shown in **Fig. 11a**, contrarily to what was reported in former research [1]. Nevertheless, the interface is not homogeneous, and local defects, such as voids, are expected as shown in **Fig. 8a** for the same fibre. Whereas, the fibre-matrix interface of steel fibres bridging cracks show a distinct structure, see **Fig. 11b-c**, characterized by significant mechanical damage, i.e. multiple cracking, and seemingly crushing at the interface.

For most of the partially-pulled fibres, there is a band of 5 – 10 µm of matrix adjacent to the fibre rich in fine-grained CH, which was surrounded by approx. 50 µm of cement paste that presented a larger porosity compared to the bulk matrix (see **Fig. 11c)**. In other cases, this region was filled with a fine-grained layer of calcite instead, as shown in **Fig. 11d**, which may be the result of the carbonation process of the abovementioned CH layer.

The source and nature of this CH-rich layer at the cracked interface is still not well understood, and there is insufficient data to allow a deep discussion on the topic. Yet, the same precipitate has been found in parallel studies on partially pulled single-fibre specimens [41], which was correlated to increases in the pull-out strength of fibres from companion specimens in [47] and to an increase of the residual tensile strength at the composite level in [4,48]. Similarly, finely grained portlandite and calcite precipitated inside micro-cracks has been reported in some

studies investigating self-healing phenomena in cracked lime-based mortar specimens [49,50], as well as at the fibre-matrix interface of glass-fibre strands in uncracked aged Glass-fibre Reinforced Concrete (GRC) [51].

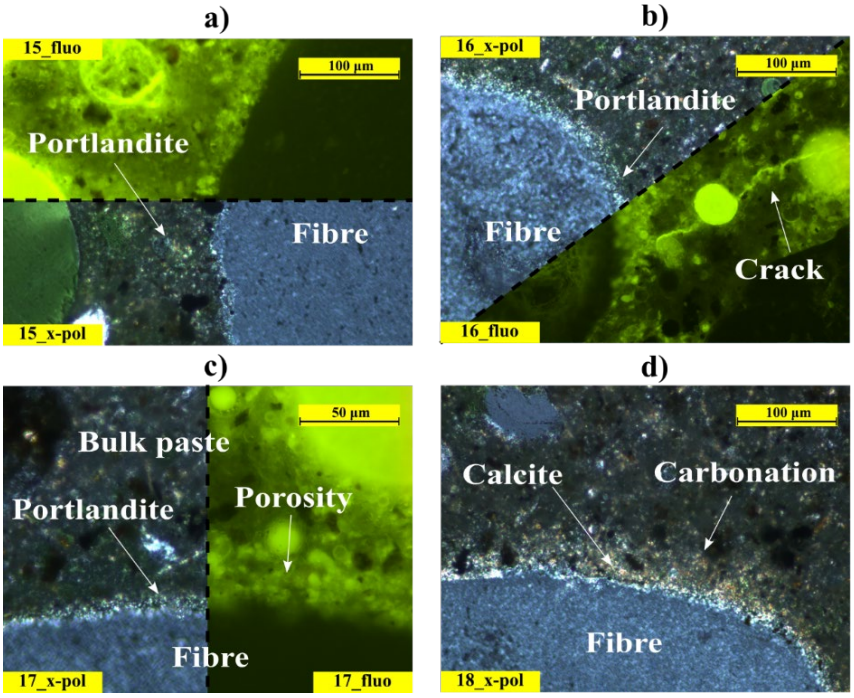

Fig. 11. Characteristics at the fibre-matrix ITZ for: a) fibre embedded in uncracked concrete matrix at 20 mm from the crack, under polarized light and UV-fluorescent light, for the specimen w30s7c0B; b) fibre crossing crack at 20 mm depth, for the specimen w30s7c0A, under cross-polarized light and UV-fluorescent light; c) closer detail of corresponding fibre presented in "b" under cross-polarized light and UV-fluorescent light; and d) carbonation at interface of embedded part of fibre adjacent to the notch, for the specimen w30s0c0A, under cross-polarized light.

5. Discussion

The data presented in the results section of this paper described the global transport in and out of the cracked SFRC. This promotes both the alteration of the matrix surrounding the crack, the precipitation of secondary phases inside the crack and eventually leads to fibre corrosion at the outermost fibres inside the crack.

In agreement with former studies [1], corresponding experiments investigating the mechanical performance of cracked SFRC have shown a substantial increase in the material toughness despite of the detrimental contribution of fibre corrosion [4]. These observations do not fully agree with former deterioration hypotheses, that associate changes in the mechanical performance primarily to fibre corrosion [2,46,52]. Therefore, more detailed conceptual deterioration models have been proposed, involving additional mechanisms, as discussed in [1]. The hypotheses proposed lead to the need of describing in more detail the processes involved in the deterioration of cracked SFRC exposed to wet-dry cycles. Since these mechanisms are often interconnected, and their analysis comprise a complex global picture.

The discussion presented below focuses on describing in detail the main mechanisms that affect the chemical and microstructural integrity of the composite based on the experimental observations presented in **Section 4**.

5.1 Conceptual deterioration model

The resulting contribution of the deterioration and recovery mechanisms described in the time-scale in **Fig. 3** are presented spatially in **Fig. 12**. The figure describes the main processes observed inside the crack at the macroscopic

level, see **Fig. 12a**, and discusses the deterioration observed at the single-fibre level in **Fig. 12b-e**, based on the hypotheses presented in [1] and supported by the data presented in this paper as discussed in the following sections.

The discussion presented below is based on the results discussed in **Section 4,** and show that deterioration and recovery processes are tightly related and occur both at the composite scale and at the fibre scale, comprising:

i) Mechanical damage of the matrix (i.e. cracking) that facilitates the transport of ions and moisture into the matrix through the main crack and along the fibres bridging the crack.

ii) Transport of ions and moisture through the matrix surrounding the crack that leads to dissolution of primary phases and formation/precipitation of secondary phases.

iii) Variation of the conditions at the steel surface (i.e. pH, concentration of Cl^-, O_2, etc.) that may lead to corrosion of the steel fibres.

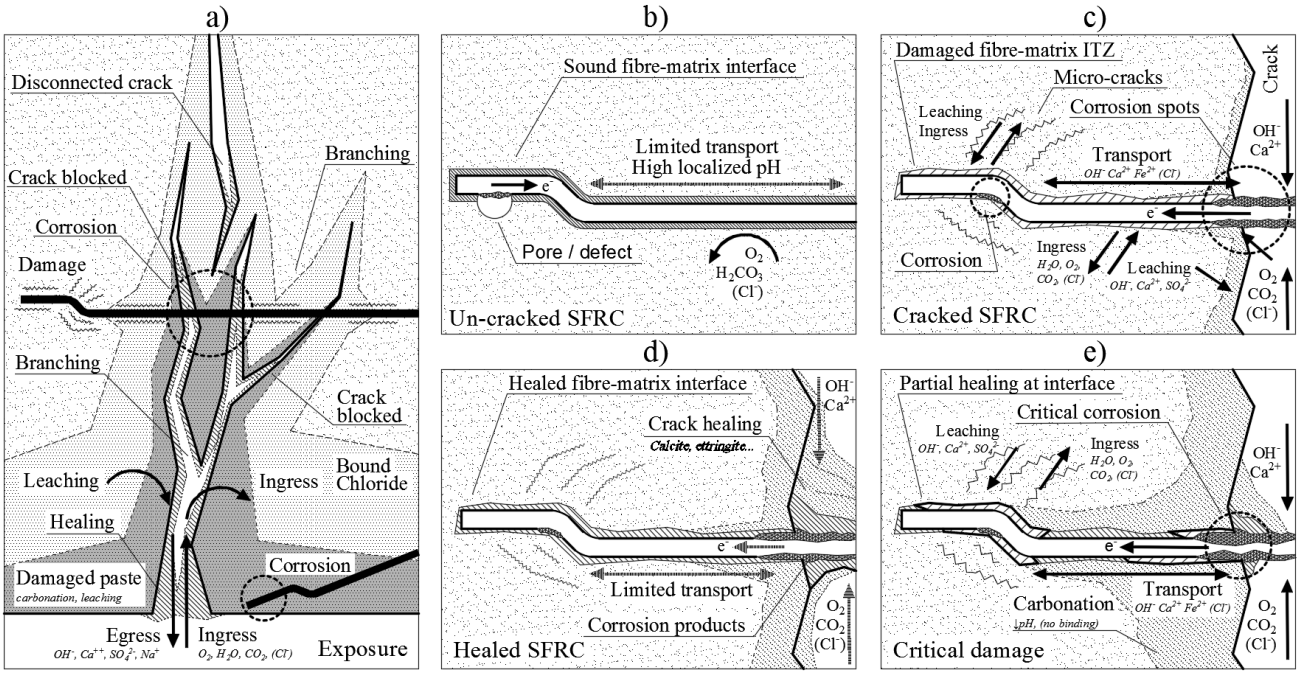

Fig. 12. Conceptual deterioration model showing: a) general processes at the composite scale (stage IV); b-e) processes at the single-fibre scale, after [1], for uncracked SFRC, at stages "I- II", (b), cracked SFRC, at stage "II" (c), healed SFRC, at stages "IV-V" (d), critical damage in cracked SFRC, at stage "III" (e) . Deterioration stages in roman numbers "I-V" refer to points marked in **Fig. 3**.

5.1.1 Composite scale

A summary of the main deterioration and recovery processes taking place in the main crack at the composite scale is presented in **Fig. 12a**, discussed in the following order: i) transport of substances, ii) reactions in the matrix surrounding the crack, iii) precipitation of secondary phases inside the crack, and iv) corrosion of steel fibres.

Cracks in concrete represent preferential paths for ionic gas and moisture transport. While, the observations reported herein indicate that steel fibres help restrain the formation of large cracks and increase the overall tortuosity of the crack, as shown schematically in **Fig. 12a**.

Ingress of extrinsic ions (e.g. Cl^-) or gasses (e.g. CO_2) and egress of intrinsic ions (e.g. OH^-, Ca^{2+}) as well as transport of moisture occur both along and transversal to the main crack, as described in **Fig. 12a**. Whereas, the bulk cement matrix provides a buffer of intrinsic ions and is able to accumulate a large amount of extrinsic ions. Transport inside the crack may be partially impeded at the crack mouth and at deeper regions of the crack, where

cracks are either: i) partially disconnected to the exterior due to branching and multiple micro-cracking, ii) not fully coalesced or locally blocked with debris, iii) locally blocked with precipitation of secondary phases.

The transport of moisture, gasses and dissolved species through the main crack leads to chemical imbalances in the pore solution of the adjacent matrix; which promotes dissolution and precipitation processes in the hardened cement paste, as depicted in **Fig. 12a**. The egress of intrinsic ions promotes the dissolution of cement phases (i.e. leaching); which weakens the matrix but also releases additional ions (e.g. Ca^{2+} or OH^-). Whereas, ingress of CO_2 promotes carbonation of the cement paste, which reduces the overall alkalinity of the solution inside the crack and transforms primary phases, e.g. converting CH and C-S-H to calcite and silica gel. In the case of exposure to chlorides, the uncarbonated matrix is able to bind a substantial amount of Cl^- (e.g. calculated ratios of water-soluble Cl^- to total Cl were in the range 1:1 – 1:4 in this study).

Additional chemical reactions to those taking place at the matrix surrounding the crack generally involve precipitation of calcite and ettringite in cracks and voids. The observed layer of precipitate was not homogeneous and did not fully close the main crack, but instead blocked the crack at discrete location, see **Fig. 12a**. In general, precipitation of secondary phases inside the crack seems to be tightly related to leaching of calcium and main cement phases from the adjacent matrix. The dissolution of primary phases and formation of secondary phases is in this case influenced by the variations in the moisture content inside the crack during the wetting and drying cycles, which alters the ionic concentration in the crack and matrix periodically, **Fig. 12a**.

Corrosion of steel fibres may result in a critical reduction of the fibre cross-section, eventually leading to a decrease in the residual mechanical performance of the composite. Corrosion of fibres embedded in uncracked SFRC occurred only on fibres that are directly exposed to the external environment (regardless of the exposure) or at some fibres near the surface under chloride exposure (i.e. outer 5 – 10 mm). Whereas, corrosion did not propagate in any case deep into the embedded parts of the steel and did not cause substantial damage to the surrounding cement matrix. Corrosion of fibres bridging cracks occurred primarily at the exposed steel surface and adjacent to the crack, typically at pH $\lessapprox$ 10, or at $[Cl^-]/[OH^-] \gtrapprox 300$ in the presence of chlorides. The discussion presented herein suggests that the pH inside the crack tends to dominate over the Cl^- concentration in terms of probability of fibre corrosion.

5.1.2 Fibre scale

Similar deterioration and recovery processes as described at the composite scale take place at the fibre scale, which are presented in **Fig. 12b-e** and are discussed in the same order.

In uncracked SFRC, steel fibres are embedded in a generally well-defined layer of cement paste, not significantly different than the bulk cement matrix but still prone to a certain extent to local defects or inhomogeneities. When the matrix cracks, the fibres bridging the main crack are partially pulled-out, which produces micro-cracking and crushing of the matrix along the fibre-matrix interface and at the deformed regions of the fibre (e.g. the hooked-end of the fibre). This network of cracks is partially connected to the main crack through the damaged interface along the stem of the fibre, as described schematically in **Fig. 12c**.

The transport processes described above at the macroscopic level extend to the crack network that originates around the fibres bridging the crack due to partial pull-out, see **Fig. 12c**. The results presented show carbonation and leaching of the cement paste surrounding the regions of the fibre crossing the crack, as shown schematically in **Fig. 12c-e**; but did not clearly indicate whether this profile progresses deep through the fibre-matrix interface. Overall, lime-rich paste is present around the damaged fibre-matrix interface of pulled fibres.

Precipitation of secondary phases, i.e. healing, at the fibre-matrix interface (i.e. small cracks 1-5 μm) is expected to seal leaching and ingress paths, see **Fig. 12d-e**. Based on previous studies (e.g. reported in [1]) and the discussion in [4], part of this healing may be responsible for substantial increase in the residual performance of the cracked

composite. The fibre-matrix interface of fibres crossing the crack showed several radial micro-cracks but minor slip-separation damage, i.e. a zone of approx. 10 – 20 µm around the fibre presented larger porosity compared to the bulk matrix. The data presented showed some sign of precipitation in these; which comprised a narrow band of approx. 2 – 5 µm composed mainly of CH around the fibre. Results presented herein provide partial evidence supporting whether this may have a direct contribution to the mechanical performance of the cracked composite after exposure; yet investigations at the single-fibre scale [41,47] confirm that these precipitation and carbonation processes at the damaged fibre-matrix interface may be responsible for a large share of the increase in pull-out strength of hooked-end fibres measured after exposure [4,53].

Corrosion of embedded fibres tends to occur at local defects at the fibre-matrix interface, such as pores or crevices, provided that locally low-pH and/or high Cl^- concentrations concur. These conditions are expected to lead to a corrosion macro-cell which did not seem to progress at fast rates in the few cases observed, see **Fig. 12b**. Inside cracks, the part of the fibre directly exposed to the solution corrodes, since the interface is damaged it may facilitate cathodic reaction and promote faster corrosion rates, see **Fig. 12d-e**. However, there were no clear signs of corrosion at the hook region of fibres embedded in the matrix, as described in previous research [46] and reported in [1].

5.2 Engineering implications

The experimental results, presented herein in the context of a conceptual deterioration model, show that the overall deterioration of the composite performance (e.g. mechanical) is not solely related to fibre corrosion; since there is substantial alteration of the cement matrix, particularly around the steel fibres bridging the crack. Therefore, potential variations of the mechanical capacity of the composite are not solely related to the reduction of the fibres' cross-section due to corrosion, but also due to an alteration of the fibre-matrix bond strength over the exposure due to chemical reactions occurring at the cement matrix surrounding the fibres.

From an engineering perspective, accounting for such variations represents a challenge that cannot be simply addressed in terms of corrosion protection/prevention measures, but needs to be understood in terms of a more complex system, where the cement matrix plays a dominant role in both the corrosion process of the steel fibres and in the alteration of the fibre-matrix bond. Therefore, the long-term mechanical performance of the cracked composite (i.e. the SFRC) under corrosive exposure depends on two parameters, i.e.: i) the tensile capacity of the steel fibres, that may decrease due to corrosion damage, and ii) the fibre-matrix bond strength that may increase or decrease depending on the alteration of the matrix surrounding the fibre. Highlighting that, these parameters are governed by transport and reaction processes occurring inside the crack and at the matrix surrounding the crack.

Engineering approaches to address this issue have been critically discussed in the context of a broader study in [27], proposing two groups of approaches: i) deem-to-satisfy approaches, where the mechanical contribution of the outermost fibres in cracked SFRC is neglected over the long-term (i.e. estimated based on experience); or ii) predictive approaches covering the individual processes described in the conceptual deterioration model presented in this paper, e.g. reactive-mass transport [54–56], electrochemical [57] and mechanical processes [53], but whose combination (to the authors' knowledge) has not been attempted so far. Nonetheless, further research investigating the individual processes described in this paper is needed to further understand and predict the overall deterioration of cracked SFRC under corrosive exposures.

6. Conclusion

This paper investigates the main processes taking place during the exposure of cracked SFRC to wet-dry cycles involving chloride and/or CO_2 exposure for one and two years. These main processes comprise changes in the cracked concrete matrix due to mass transport and the damage to the steel fibres due to corrosion. The discussion

588 presents a conceptual deterioration model that describes the deterioration and recovery mechanisms concurring
589 inside the crack.

590 The results presented show that corrosion of fibres crossing the crack occurred mainly at the steel located directly
591 in the crack and was highly influenced by the pH inside the crack, also in the presence of chlorides.

592 The deterioration model described herein, proposes that concurring dissolution and precipitation processes at the
593 crack and at the matrix surrounding it have a strong influence on the chemical composition of the solution inside
594 the crack; ultimately governing the corrosion damage of the steel fibres crossing the crack.

595 At the fibre scale, precipitation of calcite at the intersection between the fibre and the crack sealed partially the
596 surface of the steel and the damaged fibre-matrix interface was lined by a CH rich layer that may be related to
597 healing processes.

598 The findings in this paper support that the deterioration and healing processes occurring at the cement matrix of
599 cracked SFRC subject to corrosive exposures involving wet-dry cycles govern the overall deterioration of the
600 composite, which is not only due to fibre corrosion.

601 Further research focusing on quantifying the correlation of those transport and chemical processes inside cracks is
602 needed to understand and predict the long-term impact of corrosive exposures on the performance of cracked fibre
603 reinforced composites.

604 ## Acknowledgements

605 The first author would like to express his gratitude to: CowiFonden, InnovationsFonden, the German association
606 of steel fibre producers (VDS), VejDirektoratet and Mapei-Denmark, for supporting this project. The Norwegian
607 Public Roads Administration (NPRA) Ferry Free E39 coastal route project is acknowledged for funding the
608 Norwegian contribution.

609 ## References

610 [1] V. Marcos-Meson, A. Michel, A. Solgaard, G. Fischer, C. Edvardsen, T.L. Skovhus, Corrosion resistance
611 of steel fibre reinforced concrete - A literature review, Cem. Concr. Res. 103 (2018) 1–20.
612 doi:10.1016/j.cemconres.2017.05.016.

613 [2] E.S. Bernard, Durability of cracked fibre reinforced shotcrete, in: E.S. Bernard (Ed.), Shotcrete More Eng.
614 Dev. Proc. Second Int. Conf. Eng. Dev. Shotcrete, A.A. Balkema Publishers, Sydney, Australia, 2004: pp.
615 59–66.

616 [3] E.S. Bernard, Effect of Exposure on Post-crack Performance of FRC for Tunnel Segments, in: I. Vrkljan,
617 Z. Dekovic, M. Dobrilovic, J. Likar, P. Miscevic (Eds.), SEE TunnelPromoting Tunneling SEE Reg. - ITA
618 WTC 2015, ITA-AITES, Dubrovnik, Croatia, 2015: p. 13.

619 [4] V. Marcos-Meson, G. Fischer, C. Edvardsen, A. Solgaard, A. Michel, Mechanical performance of steel
620 fibre reinforced concrete exposed to chlorides and carbon dioxide: results after one year (Unpublished), J.
621 Sustain. Cem. Mater. (2018).

622 [5] C. Dauberschmidt, Untersuchungen zu den Korrosionsmechanismen von Stahlfasern in chloridhaltigem
623 Beton, Munich University, 2006.

624 [6] E. Nordström, Durability of Sprayed Concrete Steel fibre corrosion in cracks, Lulea University of
625 Technology, 2005.

626 [7] F.P. Glasser, J. Marchand, E. Samson, Durability of concrete — Degradation phenomena involving
627 detrimental chemical reactions, Cem. Concr. Res. 38 (2008) 226–246.
628 doi:10.1016/j.cemconres.2007.09.015.

[8] H. Ye, Y. Tian, N. Jin, X. Jin, C. Fu, Influence of cracking on chloride diffusivity and moisture influential depth in concrete subjected to simulated environmental conditions, Constr. Build. Mater. 47 (2013) 66–79. doi:10.1016/j.conbuildmat.2013.04.024.

[9] X. Du, L. Jin, R. Zhang, Y. Li, Effect of cracks on concrete diffusivity: A meso-scale numerical study, Ocean Eng. 108 (2015) 539–551. doi:10.1016/j.oceaneng.2015.08.054.

[10] H. Ye, N. Jin, X. Jin, C. Fu, Model of chloride penetration into cracked concrete subject to drying–wetting cycles, Constr. Build. Mater. 36 (2012) 259–269. doi:10.1016/j.conbuildmat.2012.05.027.

[11] Q.F. Liu, J. Yang, J. Xia, D. Easterbrook, L.Y. Li, X.Y. Lu, A numerical study on chloride migration in cracked concrete using multi-component ionic transport models, Comput. Mater. Sci. 99 (2015) 396–416. doi:10.1016/j.commatsci.2015.01.013.

[12] Y.C. Wu, J. Xiao, The effect of microscopic cracks on chloride diffusivity of recycled aggregate concrete, Constr. Build. Mater. 170 (2018) 326–346. doi:10.1016/j.conbuildmat.2018.03.045.

[13] J. Perko, K.U. Mayer, G. Kosakowski, L. De Windt, J. Govaerts, D. Jacques, D. Su, J.C.L. Meeussen, Decalcification of cracked cement structures, Comput. Geosci. 19 (2015) 673–693. doi:10.1007/s10596-014-9467-2.

[14] T. Ishida, P.O.N. Iqbal, H.T.L. Anh, Modeling of chloride diffusivity coupled with non-linear binding capacity in sound and cracked concrete, Cem. Concr. Res. 39 (2009) 913–923. doi:10.1016/j.cemconres.2009.07.014.

[15] Q. Yuan, C. Shi, G. De Schutter, K. Audenaert, Effect of temperature on transport of chloride ions in concrete, Concr. Repair, Rehabil. Retrofit. II. 1 (2009) 345–352.

[16] S. Alahmad, A. Toumi, J. Verdier, R. François, Effect of crack opening on carbon dioxide penetration in cracked mortar samples, Mater. Struct. Constr. 42 (2009) 559–566. doi:10.1617/s11527-008-9402-x.

[17] J. Han, W. Liu, S. Wang, D. Du, F. Xu, W. Li, G. De Schutter, Effects of crack and ITZ and aggregate on carbonation penetration based on 3D micro X-ray CT microstructure evolution, Constr. Build. Mater. 128 (2016) 256–271. doi:10.1016/j.conbuildmat.2016.10.062.

[18] D. Palin, V. Wiktor, H.M.M. Jonkers, Autogenous healing of marine exposed concrete: Characterization and quantification through visual crack closure, Cem. Concr. Res. 73 (2015) 17–24. doi:10.1016/j.cemconres.2015.02.021.

[19] M. Maes, D. Snoeck, N. De Belie, Chloride penetration in cracked mortar and the influence of autogenous crack healing, Constr. Build. Mater. 115 (2016) 114–124. doi:10.1016/j.conbuildmat.2016.03.180.

[20] T. Danner, M.R. Geiker, K. De Weerdt, μ -XRF characterisation of chloride ingress and self-healing in cracked concrete, XXIII Symp. Nord. Concr. Res. Dev. (2017) 3–6.

[21] P.D. Nieuwoudt, A.J. Babafemi, W.P. Boshoff, The response of cracked steel fibre reinforced concrete under various sustained stress levels on both the macro and single fibre level, Constr. Build. Mater. 156 (2017) 828–843. doi:10.1016/j.conbuildmat.2017.09.022.

[22] A. Bentur, S. Mindess, S. Diamond, Pull-out processes in steel fibre reinforced cement, Int. J. Cem. Compos. Light. Concr. 7 (1985) 29–37. doi:10.1016/0262-5075(85)90024-7.

[23] T.H. Ahn, D.J. Kim, S.H. Kang, Crack Self-Healing Behavior of High Performance Fiber Reinforced Cement Composites Under Various Environmental Conditions, in: Kris Zacny, R.B. Malla, W. Binienda (Eds.), Earth Sp. 2012, ASCE, Pasadena, United States, 2012: pp. 635–640.

[24] L. Ferrara, V. Krelani, F. Moretti, M. Roig Flores, P. Serna Ros, Effects of autogenous healing on the recovery of mechanical performance of High Performance Fibre Reinforced Cementitious Composites (HPFRCCs): Part 1, Cem. Concr. Compos. 83 (2017) 76–100. doi:10.1016/j.cemconcomp.2017.07.010.

[25] D. Homma, H. Mihashi, T. Nishiwaki, Self-Healing Capability of Fibre Reinforced Cementitious Composites, J. Adv. Concr. Technol. 7 (2009) 217–228. doi:10.3151/jact.7.217.

[26] European Commitee for Standardization (CEN), Fibres for concrete - Part 1: Steel fibres - Definitions, specifications and conformity, EN 14889-1:2006, European Union, 2006.

[27] V. Marcos-Meson, Durability of steel fibre reinforced concrete in corrosive environments, Technical University of Denmark, 2019.

[28] European Commitee for Standardization (CEN), Test method for metallic fibre concrete - Measuring the flexural tensile strenght (limit of proportionality (LOP), residual), EN 14651:2006 +A1, European Union, 2006.

[29] N. Otsuki, S. Nagataki, K. Nakashita, Evaluation of the AgNO3solution spray method for measurement of chloride penetration into hardened cementitious matrix materials, Constr. Build. Mater. 7 (1993) 195–201. doi:10.1016/0950-0618(93)90002-T.

[30] D.H. Campbell, R.D. Sturm, S.H. Kosmatka, Detecting Carbonation, Concr. Technol. Today (Portl. Cem. Assoc. 12 (1991) 1–6.

[31] I. The MathWorks, MATLAB Image Processing Toolbox release R2017, (2017).

[32] M. Castellote, C. Alonso, C. Andrade, P. Castro, M. Echeverría, Alkaline leaching method for the determination of the chloride content in the aqueous phase of hardened cementitious materials, Cem. Concr. Res. 31 (2001) 233–238. doi:10.1016/S0008-8846(00)00449-X.

[33] T. Chaussadent, G. Arliguie, AFREM test procedures concerning chlorides in concrete: Extraction and titration methods, Mater. Struct. 32 (1999) 230–234. doi:10.1007/BF02481520.

[34] M. Nixon, A. Aguado, Feature extraction and image processing, Featur. Extr. Image Process. Comput. Vision, Second Ed. (2008) 161–216. doi:10.1016/B978-0-12-396549-3.00001-X.

[35] M. Khanzadeh Moradllo, B. Sudbrink, Q. Hu, M. Aboustait, B. Tabb, M.T. Ley, J.M. Davis, Using micro X-ray fluorescence to image chloride profiles in concrete, Cem. Concr. Res. 92 (2017) 128–141. doi:10.1016/j.cemconres.2016.11.014.

[36] R.J. Detwiler, L.J. Powers, U.H. Jakobsen, W.U. Ahmed, K.L. Scrivener, K.O. Kjellsen, Preparing specimens for microscopy, Concr. Int. 23 (2001) 51–58.

[37] U.H. Jakobsen, L. Laugesen, N. Thaulow, Determination of water to cement ratio in hardened concrete by optical fluorescence microscopy, in: M.S. Khan (Ed.), SP-191 Water-Cement Ratio Other Durab. Parameters, 1st., American Concrete Institute (ACI), Farmington Hills, USA, 1999: pp. 27–41.

[38] U.H. Jakobsen, K. De Weerdt, M.R. Geiker, Elemental zonation in marine concrete, Cem. Concr. Res. 85 (2016) 12–27. doi:10.1016/j.cemconres.2016.02.006.

[39] J. D'Errico, Inpaint nans (Matlab), (2004).

[40] I. Markovich, J.G.M. Van Mier, J.C. Walraven, Single fiber pullout from hybrid fiber reinforced concrete, Heron. 46 (2001) 191–200.

[41] V. Marcos-Meson, A. Solgaard, T.L. Skovhus, U.H. Jakobsen, C. Edvardsen, G. Fischer, A. Michel, Pull-out behaviour of steel fibres in cracked concrete under wet-dry cycles – deterioration phenomena, Mag. Concr. Res. (2020) 1–32. doi:10.1680/jmacr.19.00448.

[42] P.S. Mangat, K. Gurusamy, Corrosion resistance of steel fibres in concrete under marine exposure, Cem. Concr. Res. 18 (1988) 44–54. doi:10.1016/0008-8846(88)90120-2.

[43] S.U. Balouch, J.P. Forth, J.-L. Granju, Surface corrosion of steel fibre reinforced concrete, Cem. Concr. Res. 40 (2010) 410–414. doi:10.1016/j.cemconres.2009.10.001.

[44] E. O'Neil, J.T. Devlin, Durability of Fiber-Reinforced Concrete Under Flexural Stress in a Severe Marine Environment, Defense Technical Information Center, Vicksburg, US, 1999.

[45] A. Beglarigale, H. Yazıcı, Electrochemical corrosion monitoring of steel fiber embedded in cement based composites, Cem. Concr. Compos. 83 (2017) 427–446. doi:10.1016/j.cemconcomp.2017.08.004.

718 [46] J.-L. Granju, S.U. Balouch, Corrosion of steel fibre reinforced concrete from the cracks, Cem. Concr. Res.
719 35 (2005) 572–577. doi:10.1016/j.cemconres.2004.06.032.

720 [47] V. Marcos-Meson, A. Solgaard, G. Fischer, C. Edvardsen, A. Michel, Pull-out behaviour of hooked-end
721 steel fibres in cracked concrete exposed to wet-dry cycles of chlorides and carbon dioxide – Mechanical
722 performance, Constr. Build. Mater. 240 (2020) 117764. doi:10.1016/j.conbuildmat.2019.117764.

723 [48] V. Marcos-Meson, Durability of steel fibre reinforced concrete in corrosive environments. Chapter 3,
724 Technical University of Denmark, 2019.

725 [49] B. Lubelli, T.G. Nijland, R.P.J. Van Hees, Self-healing of lime based mortars: microscopy observations on
726 case studies, in: Proc. First Int. Conf. Self Heal. Mater., Springer, Noordwijk aan Zee, NL, 2011.

727 [50] T.G. Nijland, J. a Larbi, R.P.J. Van Hees, B. Lubelli, Self Healing Phenomena in Concretes and Masonry
728 Mortars: A Microscopic Study, in: A.J.M. Schmets, S. van der Zwaag (Eds.), First Int. Conf. Self Heal.
729 Mater., Springer, Noordwijk aan Zee, NL, 2007: pp. 76–91.

730 [51] P. Purnell, N.. Short, C.. Page, A.. Majumdar, Microstructural observations in new matrix glass fibre
731 reinforced cement, Cem. Concr. Res. 30 (2000) 1747–1753. doi:10.1016/S0008-8846(00)00407-5.

732 [52] C. Frazão, J. Barros, A. Camões, A.C. Alves, L. Rocha, Corrosion effects on pullout behavior of hooked
733 steel fibers in self-compacting concrete, Cem. Concr. Res. 79 (2016) 112–122.
734 doi:10.1016/j.cemconres.2015.09.005.

735 [53] V. Marcos-Meson, G. Fischer, A. Solgaard, C. Edvardsen, A. Michel, Mechanical performance and
736 corrosion damage of steel fibre reinforced concrete – A multiscale modelling approach, Constr. Build.
737 Mater. 234 (2020) 117847. doi:10.1016/j.conbuildmat.2019.117847.

738 [54] A. Michel, V. Marcos-Meson, M. Geiker, Microstructural changes and mass transport in cement-based
739 materials: a modeling approach (Unpublished), Cem. Concr. Res. (2019).

740 [55] M.M. Jensen, B. Johannesson, M. Geiker, A Coupled Chemical and Mass Transport Model for Concrete
741 Durability, in: n.d. doi:10.4203/ccp.100.17.

742 [56] A. Michel, V.M. Meson, H. Stang, M.R. Geiker, M. Lepech, Coupled mass transport, chemical, and
743 mechanical modelling in cementitious materials: A dual-lattice approach, in: R. Caspeele, L. Taerwe, D.M.
744 Frangopol (Eds.), Life Cycle Anal. Assess. Civ. Eng. Towar. an Integr. Vis. Proc. Sixth Int. Symp. Life-
745 Cycle Civ. Eng. (IALCCE 2018), CRC Press, Ghent, Belgium, 2018: pp. 965–972.

746 [57] A. Michel, Reinforcement Corrosion: Numerical Simulation and Service Life Prediction, 2012.

747 [58] F. He, C. Shi, Q. Yuan, C. Chen, K. Zheng, AgNO3-based colorimetric methods for measurement of
748 chloride penetration in concrete, Constr. Build. Mater. 26 (2012) 1–8.
749 doi:10.1016/j.conbuildmat.2011.06.003.

750 [59] F. He, C. Shi, Q. Yuan, K. Zheng, Q. Zou, Factors influencing chloride concentration at the color change
751 boundary using AgNO3 colorimetric method, Kuei Suan Jen Hsueh Pao/ J. Chinese Ceram. Soc. 36 (2008).

752

Appendix A

This appendix contains the processed experimental results from the studies carried out in this paper.

A.1. Fibre counting, chloride and pH profiles

The results from the fibre counting after one- and two-year exposure are presented in **Fig. 13**, as discrete points for each fibre of each sample, classified by colour according to the degree of damage (see **Fig. 1**). The figure shows a surface of 75 x 125mm, corresponding to the original surface of the crack (150 x 125 mm) divided by its vertical symmetry axis. The edges exposed to the solution are marked in red (lower, left and upper edges). Furthermore, the crack width is shown at the right axis, including an estimation of the position of the neutral axis at 35 mm and 25 mm from the upper face for the 0.15 mm and 0.30 mm samples respectively, which was calculated based on [4], see **Fig. 13**. Profiles are presented by a closed polygon corresponding to the 95% confidence interval of the boundary for each sample for the following colorimetric tests: a) free chloride profiles, based on the $AgNO_3$ spray test, i.e. free Cl^- ≷ 70 - 140 mmol/l [58,59], shown in brown; b) pH profiles from the phenolphthalein spray test, i.e. pH > 9, shown in purple for the samples exposed to chlorides; and c) pH profiles from universal indicator spray test, for pH > 11, shown in blue for the samples not exposed to chlorides.

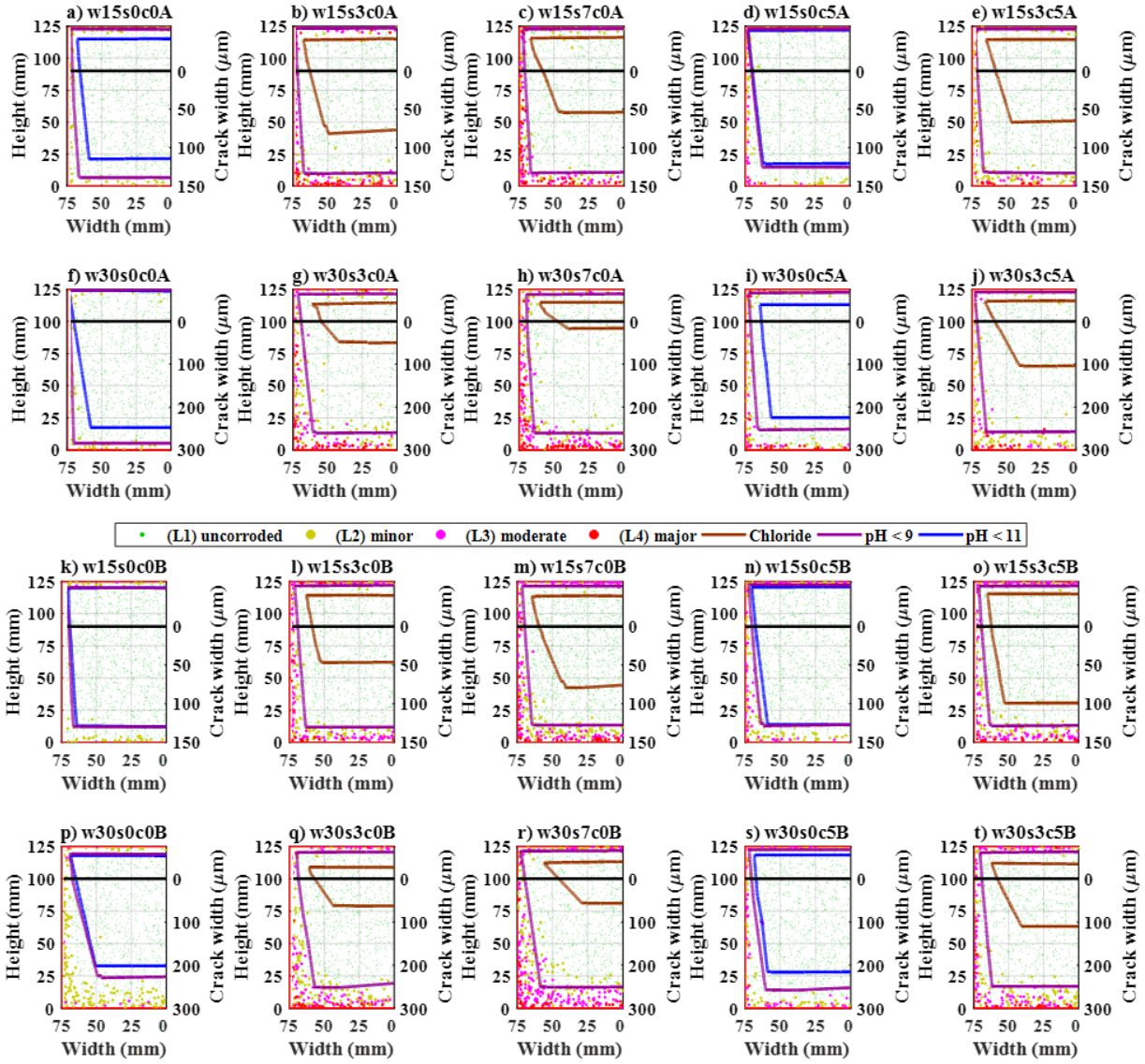

Fig. 13. Location of fibres and colorimetric profiles after one-year exposure for: a,f) cracked reference, s0c0; b,g) 3.5% NaCl exposure, s3c0; c,h) 7.0% NaCl exposure, s7c0; d,i) CO_2 exposure, s0c5; e,j) 3.5% NaCl and CO_2 exposure, s3c5. And results after two-years exposure for: k,p) cracked reference, s0c0; l,q) 3.5% NaCl exposure, s3c0; m,r) 7.0% NaCl exposure, s7c0; n,s) CO_2 exposure, s0c5; o,t) 3.5% NaCl and CO_2 exposure, s3c5. The fibres are classified according to corrosion level (levels 1 – 4), and the profiles plotted correspond to the mean value at 95% confidence (i.e. normal distribution).

A.2. Water soluble chloride profiles

The concentration of water-soluble chlorides ($[Cl^-]_{ws}$) measured after one- and two-years of exposure are presented in **Fig. 14**, as contours of water-soluble chlorides expressed as the relative weight to the hardened binder (i.e. mg/g). The figure shows the face of the crack split by its vertical symmetry axis, i.e. 75 x 125 mm, displaying on the horizontal axis the distance to the centre of the crack and on the left-vertical axis the depth inside the crack (i.e. the height of the specimen). Additionally, the right-vertical axis shows the crack width, expressed in µm; whereas, the neutral axis, where the crack width is zero, is represented as a dotted horizontal line. The exposed edges (i.e. top, bottom and right) are marked in a red dotted line.

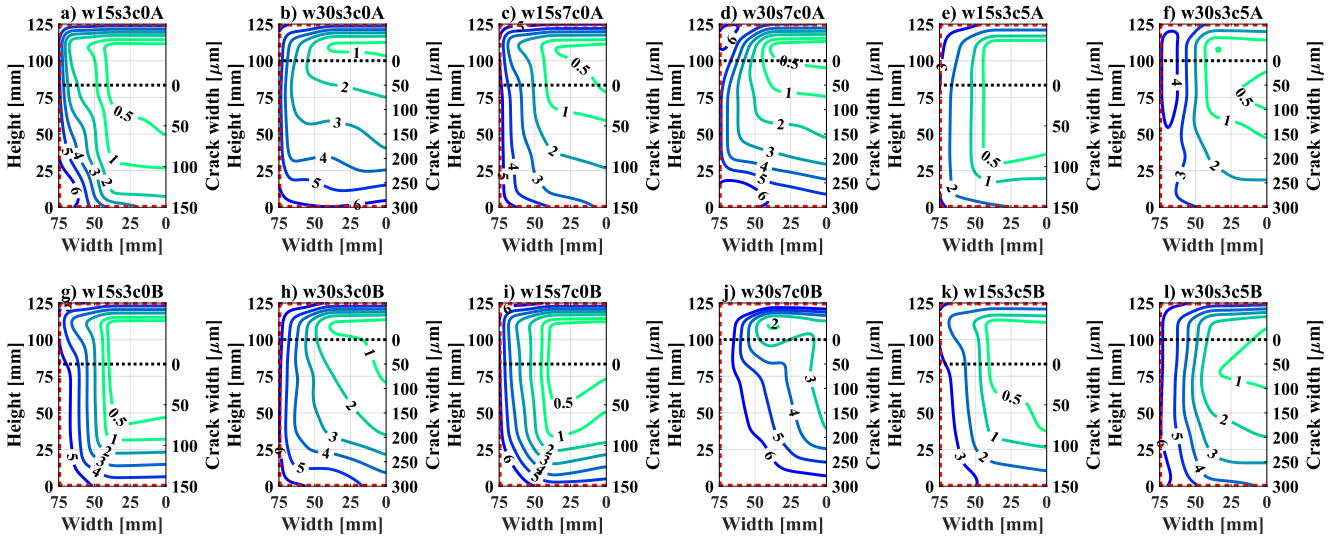

Fig. 14. Contour plots of water-soluble chloride profiles (mg/g) at the crack surface after one-year for: a,b) 3.5 wt.% NaCl exposure cracked at 0.15 and 0.3 mm, w15s3c0A and w30s3c0A; c,d) 7 wt.% NaCl exposure cracked at 0.15 and 0.3 mm, w15s7c0A and w30s7c0A; e,f) 3.5 wt.% NaCl and CO_2 exposure cracked at 0.15 and 0.3 mm, w15s3c5A and w30s3c5A. And contours after two-years exposure, for: g,h) 3.5 wt.% NaCl exposure cracked at 0.15 and 0.3 mm, w15s3c0B and w30s3c0B; i,j) 7 wt.% NaCl exposure cracked at 0.15 and 0.3 mm, w15s7c0B and w30s7c0B; k,l) 3.5 wt.% NaCl and CO_2 exposure cracked at 0.15 and 0.3 mm, w15s3c5B and w30s3c5B. Locations of extraction points are given in **Fig. 2b.**

A.3. Elemental chlorine profiles transversal to the crack

The total elemental chlorine (Cl) present in the cement matrix was measured by µ-XRF spectroscopy mapping, as described in **Section 3.5**. The results presented in **Fig. 15** show the total Cl content in the cement paste (expressed in wt.%) on a cut-section transverse to the crack (i.e. along the x-y axis of the beam according to **Fig. 2a**), at the centre of the specimens.

The results presented correspond to specimens exposed to wet-dry cycles at 7 wt.% NaCl during one- (**Fig. 15a**) and two-years (**Fig. 15b**) respectively. The depth of the $[Cl^-]_{ws}$ profile into the uncracked exposed surface (e.g. at the matrix around the notch) progresses substantially with time, and Cl content as high as 1 – 2 wt.%-cem are measured at the outer 10 – 15 mm over two years. The evolution of the Cl profile of the specimen exposed during two-years (**Fig. 15b**) compared to the one exposed for one year (**Fig. 15a**) shows that the matrix surrounding the crack could absorb as well a substantial amount of Cl within one-year of exposure, and that transport of Cl^-

transversal to the crack into the bulk matrix plays a leading role in the overall transport of Cl^- through the crack, i.e. the bulk matrix surrounding the crack acts as a buffer where the Cl^- that ingresses into the crack is transported and bound.

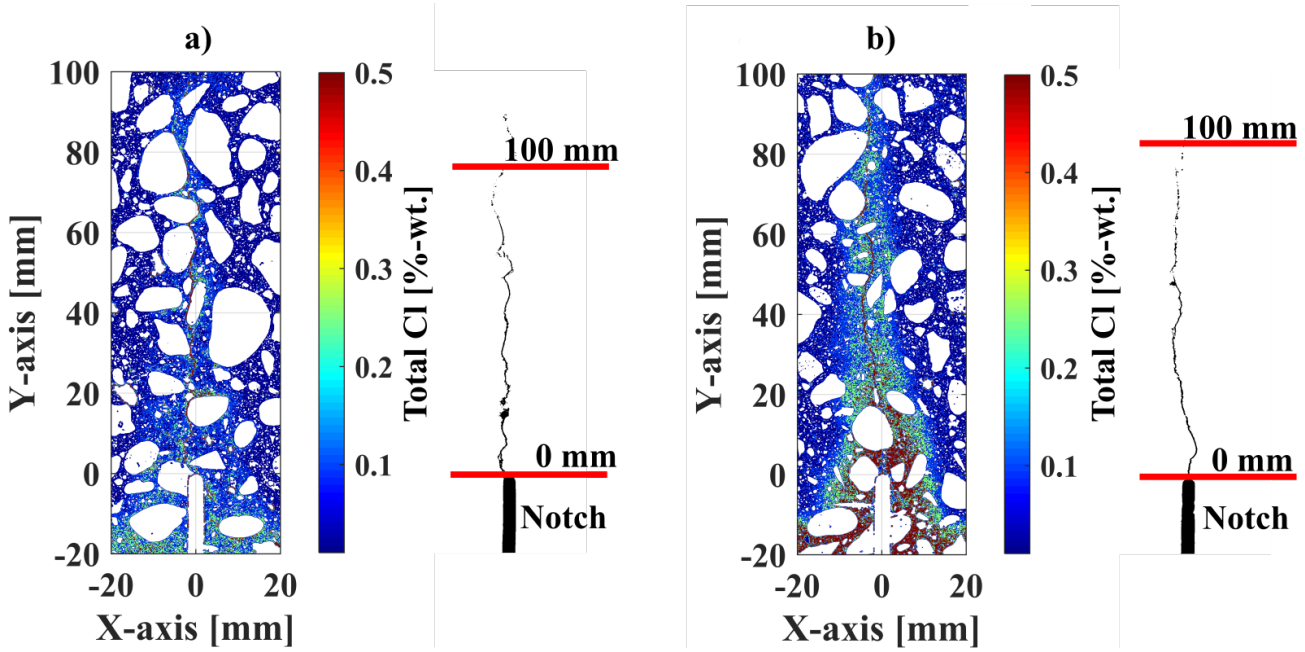

Fig. 15. Total chlorine concentration maps and segmented crack profiles for specimens cracked at 0.3mm exposed to 7 wt.% NaCl (w30s7c0) during: a) one-year (w30s7c0A); and b) two-years (w30s7c0B). The filled contours were plotted in Cl wt.%, with thresholds at: 0, 0.1, 0.25 and 0.5 wt.%.

A.4. Petrographic study

A petrographic study was carried out to assess the extent of deterioration of the cracked specimens exposed to wet-dry cycles, focusing on the state of the matrix and fibres in the outer region of the crack. The study comprised the inspection of four specimens cracked at 0.3 mm and exposed to wet-dry cycles during one and two years. The specimens were extracted at the central section of the beam and covered the outer 40 mm of the crack, see **Fig. 16a**. The specimens are presented as a scanned image of the thin-section under polarized light, being: i) a specimen exposed to wet-dry cycles of limewater for one year, w30s0c0A (**Fig. 16b**); ii) a specimen exposed to wet-dry cycles of 7 wt.% of NaCl for one year, w30s7c0A (**Fig. 16c**); iii) a specimen exposed to wet-dry cycles of fresh water and CO_2 for two years, s0c5B (**Fig. 16d**); and iv) a specimen exposed to wet-dry cycles of 7 wt.% of NaCl for two years, w30s7c0B (**Fig. 16e**). Additionally, a specimen was extracted at the centre (i.e. at approx. 60mm from the exposed faces) of an uncracked beam, exposed to wet-dry cycles of limewater for two years, w0s0c0B (**Fig. 16f**).

The images presented in **Fig. 16** are been complemented with annotations regarding the location of areas which are examined and discussed in **Section 5**, see squares and text in magenta. The boundary where the precipitate inside the main crack does not comprise mostly carbonates has been marked with a blue line. Additionally, the position of the steel fibres intersecting the thin-section have been marked with a red circumference and the estimated orientation of fibres inclined relative to the crack has been marked with a dotted red line. A brief description of each section is given below.

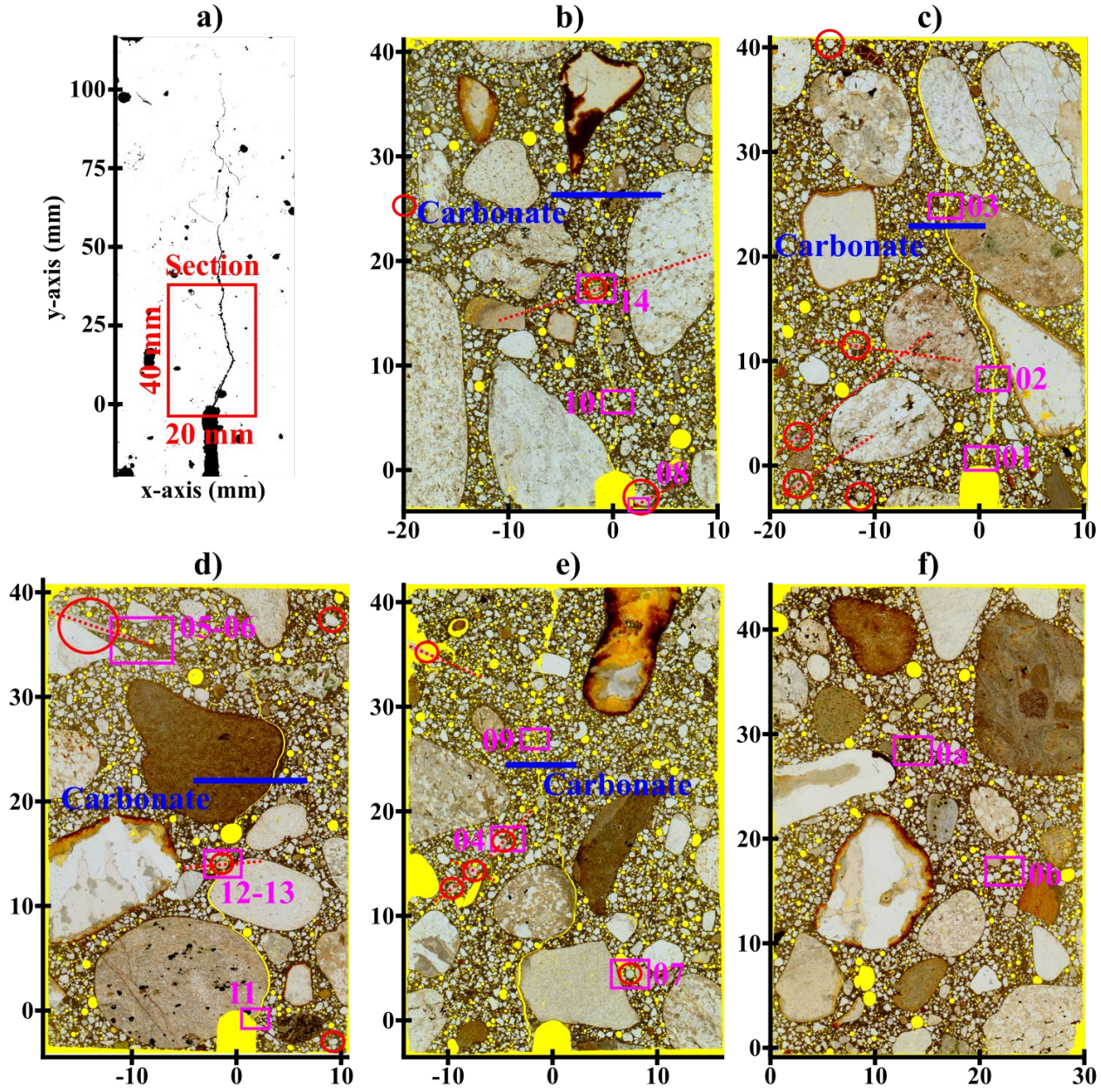

Fig. 16. Overview of thin-sections with study regions: a) schematic of location of thin-section at the crack; b) cracked specimen exposed to limewater cycles for one year, w30s0c0A; c) cracked specimen exposed to cycles of 7 wt.% NaCl for one year, w30s7c0A; d) cracked specimen exposed to cycles of fresh water and CO_2 for two years, w30s0c5B; e) cracked specimen exposed to cycles of 7 wt.% NaCl for two years, w30s7c0B; f) uncracked specimen exposed to limewater cycles for two years, w0s0c0B. The location of steel fibres is marked with a red circle, the areas investigated in the discussion section are marked in magenta and numbered and the depth of carbonation inside the crack is marked as a blue dashed line.

The cracked specimen exposed to wet-dry cycles of limewater for one year, i.e. w30s0c0A, is shown in **Fig. 16b**. The investigated section shows precipitation of secondary phases in the outer 30 mm of the main crack, primarily ettringite and calcite that does not close the crack mouth at the notch. Deeper inside the crack, precipitation of secondary phases occurs at discrete spots and comprises mostly ettringite. There is a fibre intercepting the crack at 15 mm inside the crack and the matrix surrounding the crack presents multiple cracking and branching. Additional branching is observed at 30 mm inside the crack, which disconnects the crack and is partly closed by

secondary phases. Furthermore, there are two fibres intercepting the notch that are directly exposed to the surface. Corrosion is observed at the exposed areas of the steel.

The cracked specimen exposed to wet-dry cycles of 7% NaCl for one year, i.e. w30s7c0A, is shown in **Fig. 16c**. The analysis of the section indicates substantial precipitation of secondary phases up to 25 mm inside the crack, comprising mostly ettringite and calcite; the precipitate covers only a few μm inside the crack but closes almost fully the crack mouth, which is partially blocked with debris. Secondary phases precipitate locally deeper inside the crack, comprising mostly ettringite. The crack runs almost continuous through the whole section, up to 40 mm, where it is partially disconnected due to branching. There is a cluster of four fibres at the bottom-left corner, i.e. at 10 – 15 mm from the notch; three of these fibres were crossing the crack at a different plane from the sectioned, as observed in the counterparts resulting from the preparation of the thin section.

The cracked specimen exposed to wet-dry cycles of fresh water and CO_2 for two years, i.e. w30s0c5B, is shown in **Fig. 16d**. The studied section shows precipitation of secondary phases (e.g. mainly ettringite and calcite) at the crack faces within the outer 25 mm of the crack, not covering the cracked section (i.e. approx. 10 μm inside the crack), but fully closing the crack mouth. There is a fibre intersecting the crack at a depth of approx. 15 mm, which results in branching of the crack upstream and multiple cracking of the surrounding matrix. A second fibre, inclined relative to the crack, is located at the upper-left side of the section, i.e. at approx. 40 mm into the crack; which corresponds to the branching and multiple cracking observed at the main crack, near the estimated interception region with the main crack.

The cracked specimen exposed to wet-dry cycles of 7% NaCl for two years, i.e. w30s7c0B, is presented in **Fig. 16e**. The section shows that at this location the crack mouth does not fully connect to the external environment in this case. Precipitation of secondary phases inside the crack is similar to the previous cases. There is a cluster of four fibres at approx. 15 mm inside the crack. Two of the fibres are inclined relative to the crack and are expected to intersect the crack at other planes; contributing to the crack-branching observed at 15 – 20 mm inside the crack. A fibre inclined with respect to the crack, is located at the upper-left side of the section; corresponding to the branching and micro-cracking observed at approx. 30 mm inside the crack, which follows the expected trajectory of the fibre.

The uncracked specimen exposed to wet-dry cycles of limewater for two years, i.e. w0s0c0B, is presented in **Fig. 16f**. The section is used as a reference to evaluate the state of the cement paste and compare changes due to exposure (e.g. using the inspection areas 0a and 0b in **Fig. 16f**). The analysis shows that there is a significant change in the coloration of the cement paste of the cracked specimens relative to this reference. The reference specimen shows a clear identification of primary phases under cross-polarized light and a substantial content of portlandite, which is not apparent in the previous ones.